Modeling and Simulation of Mixture Flows : Application to Powder-Snow Avalanches

Caterina Calgaro, Emmanuel Creusé, Thierry Goudon

To cite this version:

Caterina Calgaro, Emmanuel Creusé, Thierry Goudon. Modeling and Simulation of Mixture Flows : Application to Powder-Snow Avalanches. Computers and Fluids, 2015, 107, pp.100-122. ⟨hal-00732112v2⟩

HAL Id: hal-00732112
https://hal.science/hal-00732112v2
Submitted on 23 Oct 2014

Modeling and Simulation of Mixture Flows : Application to Powder–Snow Avalanches

Caterina Calgaro [*] Emmanuel Creusé [*] Thierry Goudon [†]

February 1, 2015

Abstract

We are concerned with the numerical simulation of certain multi-fluids flows, which in particular arise in the modeling of powder–snow avalanches. The behavior of the mixture is described through a single mass density and a velocity field, with an unusual constraint that relates the divergence of the velocity to derivatives of the density. We discuss a derivation of the model from a Eulerian-Lagrangian description of the mixture. We propose a numerical scheme based on a hybrid Finite Volume/Finite Element method. This approach is validated by comparison to analytical solutions, numerical solutions and experimental data. The scheme works on unstructured meshes and it can be advantageously coupled to mesh refinements strategies in order to follow fronts of high density variation. We explore numerically the role of the leading coefficients that characterize the flow: the Froude, the Reynolds and the Schmidt numbers.

Keywords : Variable density flows. Mixture flows. Finite Volume method. Finite Element method. Unstructured meshes. Particulate flows and hydrodynamic regimes.

Introduction

We are concerned with systems of PDEs describing the evolution of mixture flows. The fluid is described by the density $\rho(t,x) \geq 0$, depending on time $t \geq 0$ and space $x \in \Omega \subset \mathbb{R}^N$, and the velocity field $u(t,x) \in \mathbb{R}^N$. These quantities obey mass conservation and momentum balance, respectively, which read

$$\partial_t \rho + \nabla_x \cdot (\rho u) = 0, \tag{1}$$

---

[*] Université Lille 1 - Laboratoire Paul Painlevé and E.P.I. MEPHYSTO - INRIA Lille Nord Europe, Cité scientifique, 59655 Villeneuve d'Ascq Cedex, France. `caterina.calgaro@math.univ-lille1.fr`, `emmanuel.creuse@math.univ-lille1.fr`

[†] E.P.I. COFFEE - INRIA Sophia Antipolis Méditerranée, 2004, route des Lucioles - BP 93, 06902 Sophia Antipolis Cedex & Labo. J. A. Dieudonné, CNRS-Université Nice Sophia Antipolis, UMR 7351, Parc Valrose 06108 Nice cedex 02, France. `thierry.goudon@inria.fr`

and

$$\partial_t(\rho u) + \mathrm{Div}_x(\rho\ u \otimes u) + \nabla_x p = \rho g + \mathrm{Div}_x\big(2\mu \mathbb{D}(u)\big) \tag{2}$$

with $\mathbb{D}(u) = (\nabla_x u + \nabla_x u^T)/2$. In (2), g stands for the gravity acceleration (but it can include further external forces), while μ represents the dynamic viscosity of the fluid. This positive quantity might depend on the density ρ as we shall detail below. The originality of the modeling of mixtures relies on the definition of the pressure p. It is associated to the non–standard constraint

$$\nabla_x \cdot u = -\nabla_x \cdot \big(\kappa \nabla_x \ln(\rho)\big) \tag{3}$$

where κ is a positive coefficient. Of course, when $\kappa = 0$ the system (1)–(3) is nothing but the usual Incompressible Navier–Stokes system. In this specific case, we have $\nabla_x \cdot u = 0$ and the density remains constant along the characteristic curves $(t, x) \mapsto X(t, x)$ of the flow:

$$\frac{\mathrm{d}}{\mathrm{d}t}\big[\rho(t, X(t, x))\big] = 0, \qquad \frac{\mathrm{d}}{\mathrm{d}t}X(t, x) = u(t, X(t, x)), \qquad X(0, x) = x$$

(as long as u is smooth enough and the definition of X makes sense). Accordingly, when the fluid is initially homogeneous, it remains homogeneous for ever. Dealing with non–homogeneous flows, the system (1)–(2) with $\nabla_x \cdot u = 0$ couples equations of different types and it presents specific difficulties, both for mathematical analysis and numerical simulation. For instance, a fine analysis of the well-posedness issues can be found in [19, 22] and for further results and comments we refer the reader to [7, Chapter 6, Section 2] or [51, Chapter 2]. Similarly, the numerical treatment is by no way a mere adaptation of the homogeneous case, see [14, 16] and the references therein. In this paper, we shall consider the case $\kappa > 0$ and we wish to construct numerical methods able to handle this non–standard coupling.

The Fick law (3) relating the divergence of the velocity field to derivatives of the density has been introduced in [42, 47] and it has been further developed in [11, 36, 46, 61] for modeling flows where species (like salt or pollutant) are dilute in a compressible or incompressible fluid. The mixture is seen as an averaged continuum, described by a single pair density–velocity field. Therefore, the density ρ is naturally highly non homogeneous, and the constitutive law (3) accounts for diffusion effects between the constituents of the mixture. It is worth pointing out that the model has been independently discussed as a correction to the standard fluid mechanics, even for single-phase flows [9, 12] (and for analysis reasonings that bring out remarkable mathematical structures of the corrected system, see [34]). In this work, we are particularly interested in the application of the model to reproduce powder–snow avalanches, as it has been proposed in [24, 27, 30, 55, 56]. Questions of existence and uniqueness of solutions are investigated in [6, 47, 64, 65, 49] and [5, Chapter 3, Section 4]. The analysis has been completed recently in [13, 50] by using energy estimates available when a specific relation holds between the viscosity μ and the coefficient κ (see below), and in [44] where the numerical analysis viewpoint is developed from a Finite Element approximation. It is worth mentioning that (1)–(2) completed with the constraint (3) shares many features with low Mach models which arise in combustion theory. In low Mach models the logarithm in (3) is replaced by another function of the density. We refer the reader to [52, Section 8.8] for a sketch of analysis on weak solutions, see also [20, 49], and to [1, 2] for further details on low Mach regimes. We shall go back to these questions elsewhere; here we focus on the difficulties introduced by the constraint (3) and applications to mixture flows.

The purpose of this paper is two–fold. On the one hand, we propose an overview of the modeling issues, and we bring out the role of certain simplifying hypotheses. It allows to construct a hierarchy of models. On the other hand, we propose a dedicated numerical method for the simulation of such mixture flows, paying a specific attention to the simulation of powder-snow avalanches. Comparison with other numerical simulations and experimental data demonstrate the relevancy of the model and of the numerical techniques. In Section 1 we review the basis of the derivation of the system (1)–(3) when describing mixture flows. In particular, we clarify the fact that different formulations of the problem can be naturally used and we present a hierarchy of models with gradual difficulties for numerics — and certainly for mathematical analysis too. This discussion is completed by an Appendix where we detail how the constitutive law can be derived from the Eulerian–Lagrangian modeling of particulate flows, in a certain hydrodynamic regime. This derivation might open new perspectives, with models involving generalized closure relations [41]. Section 2 is mainly devoted to the numerical simulation of avalanche phenomena. Firstly, we detail in Section 2.1 the principles of the numerical method we propose to solve the system. A hybrid scheme is introduced, which combines a Finite Volume method for solving the mass conservation equation to a Finite Element method for solving the momentum balance equation and the constraint. This strategy is directly inspired from our works [16, 14] on incompressible flows. We point out that the scheme works on unstructured meshes, thus it is well adapted to incorporate mesh refinement procedures. In turn, the scheme is quite efficient in capturing displacements of fronts, characterized by high variation of the density, a typical feature of powder–snow avalanches. Secondly, in Section 2.2, we check through numerical experiments and direct comparison with analytical solutions the accuracy properties of the scheme. Thridly, Section 2.3 is concerned with the simulation of realistic avalanche phenomena, and we can compare the numerical tests to other results available in the literature, obtained with completely different numerical strategies, possibly based on the use of commercial softwares, or coming from laboratory experiments. It turns out that the Froude, the Reynolds and the Schmidt numbers are the key parameters that govern the flow, and grade the numerical difficulty. Finally, in Section 2.4, we investigate the role of these parameters, based on numerical grounds.

1 Modeling of Mixtures

In this Section, we review various aspects of the derivation of the system (1)–(3). To this end, let us introduce a few notation. We assume that the mixture is made of a disperse phase interacting with a dense phase, but we shall adopt an averaged description of the flow. The two fluids that constitute the mixture are characterized by their reference mass density: we denote $\bar{\rho}_f$ the density of the dense phase and $\bar{\rho}_d$ the density of the dilute phase. We also need the velocity field of each constituent: $u_f(t, x)$ and $u_d(t, x)$, respectively. We define the volume fraction of the disperse phase $0 \leq \phi(t, x) \leq 1$:

$$\phi(t, x) = \lim_{r \to 0} \frac{\text{Volume occupied at time } t \text{ by the disperse phase in } B(x, r)}{|B(x, r)|}.$$

Therefore, assuming that each phase is incompressible and keeps a constant mass density, the density of the mixture is defined by the convex combination

$$\rho(t,x) = \underbrace{\bar{\rho}_f\big(1-\phi(t,x)\big)}_{:=\rho_f(t,x)} + \underbrace{\bar{\rho}_d\phi(t,x)}_{:=\rho_d(t,x)} = \bar{\rho}_f + (\bar{\rho}_d - \bar{\rho}_f)\phi(t,x). \tag{4}$$

We can write the mass conservation for the two phases

$$\partial_t \rho_f + \nabla_x \cdot (\rho_f u_f) = 0 = \partial_t \rho_d + \nabla_x \cdot (\rho_d u_d).$$

Accordingly we obtain

$$\partial_t \rho + \nabla_x \cdot (\rho u) = 0 \tag{5}$$

where

$$\rho u(t,x) = (\rho_f u_f + \rho_d u_d)(t,x),$$

defines the *mean mass velocity* (or barycentric velocity) $u(t,x)$. Note that, even if the two constituents are incompressible, u is not divergence free, by contrast to the *mean volume velocity*

$$v(t,x) = \big(1-\phi(t,x)\big)u_f(t,x) + \phi(t,x)u_d(t,x).$$

Indeed, the velocity field v is solenoidal because

$$\begin{aligned}\partial_t\Big(\frac{\rho_f}{\bar{\rho}_f} + \frac{\rho_d}{\bar{\rho}_d}\Big) &= \partial_t(1-\phi+\phi) = 0\\ &= -\nabla_x \cdot \Big(\frac{\rho_f u_f}{\bar{\rho}_f} + \frac{\rho_d u_d}{\bar{\rho}_d}\Big) = -\nabla_x \cdot v = 0.\end{aligned}$$

Next, we write the usual momentum equation for ρu, that is

$$\partial_t(\rho u) + \mathrm{Div}_x(\rho\, u \otimes u) + \nabla_x p = \rho g + \mathrm{Div}_x(2\mu \mathbb{D}(u))$$

with $\mathbb{D}(u) = (\nabla_x u + \nabla_x u^T)/2$. The definition of the pressure p comes from a constitutive relation which postulates a Fick law between u, v and ρ.

1.1 The Kazhikhov–Smagulov Model

According to Kazhikhov and Smagulov [47] we set

$$u = v - \kappa \nabla_x \ln(\rho),$$

for some constant $\kappa > 0$. This Fick's law describes the diffusive fluxes of one fluid into the other [46, 61]. Clearly, this relation yields (3). In [36], it is found convenient to derive the Kazhikhov-Smagulov relation from a similar relation for the fields associated to the dense phase, namely

$$u_f = u - \kappa \nabla_x \ln(\rho_f/\rho).$$

Here, we point out another relation, involving the evolution of the volume fraction.

Lemma 1 *Let the mixture density* ρ *be defined by* (4)*. It satisfies the mass conservation* (5) *and the following assertions are equivalent:*

i) There exists $\kappa > 0$ *and a solenoidal field* v *such that* $u = v - \kappa\nabla_x \ln(\rho)$*,*

ii) There exists $\tilde{\kappa} > 0$ *such that the volume fraction* ϕ *satisfies the convection–diffusion equation*

$$\partial_t\phi + \nabla_x \cdot (\phi u) = \nabla_x \cdot \big(\tilde{\kappa}\nabla_x \ln\big(\bar{\rho}_f + (\bar{\rho}_d - \bar{\rho}_f)\phi\big)\big).$$

Proof. We rewrite the mass conservation (5) as follows

$$\begin{aligned}\partial_t\big(\bar{\rho}_f + (\bar{\rho}_d - \bar{\rho}_f)\phi\big) + \nabla_x \cdot \Big(\big(\bar{\rho}_f + (\bar{\rho}_d - \bar{\rho}_f)\phi\big)u\Big) &= 0\\ = (\bar{\rho}_d - \bar{\rho}_f)\Big(\partial_t\phi + \nabla_x \cdot (\phi u)\Big) + \bar{\rho}_f\nabla_x \cdot u.\end{aligned}$$

Let us assume that $i)$ holds. Since v is divergence free, we obtain

$$\partial_t\phi + \nabla_x \cdot (\phi u) = \frac{\bar{\rho}_f}{\bar{\rho}_d - \bar{\rho}_f}\nabla_x \cdot \Big(\kappa\nabla_x \ln\big(\bar{\rho}_f + (\bar{\rho}_d - \bar{\rho}_f)\phi\big)\Big) = \frac{\bar{\rho}_f}{\bar{\rho}_d - \bar{\rho}_f}\nabla_x \cdot \big(\kappa\nabla_x \ln(\rho)\big).$$

Hence $ii)$ holds with $\tilde{\kappa} = \kappa\frac{\bar{\rho}_f}{\bar{\rho}_d - \bar{\rho}_f}$. Conversely, assuming $ii)$, the mass conservation imposes

$$\nabla_x \cdot u = -\frac{\bar{\rho}_d - \bar{\rho}_f}{\bar{\rho}_f}\nabla_x \cdot \Big(\tilde{\kappa}\nabla_x \ln\big(\bar{\rho}_f + (\bar{\rho}_d - \bar{\rho}_f)\phi\big)\Big) = -\frac{\bar{\rho}_d - \bar{\rho}_f}{\bar{\rho}_f}\nabla_x \cdot \big(\tilde{\kappa}\nabla_x \ln(\rho)\big).$$

We conclude that $i)$ holds. □

This statement is important because it implies that different choices of unknowns are equivalent which, in turn, can motivate different numerical strategies. Indeed, instead of working with density ρ and velocity u as numerical unknowns like in [24], it is equally relevant to solve the evolution PDEs for ϕ and u, using $\rho = \bar{\rho}_f + (\bar{\rho}_d - \bar{\rho}_f)\phi$. The alternative parallels with Zero-Mach flows, where we can work either with the mass density or the temperature as primary unknown. Then the mass conservation (5) appears as the constraint that defines the pressure. We refer the reader to [4, 27, 30] where this viewpoint is adopted. Beyond the description of mixture flows, the interested reader can find in Brenner's papers [9, 10, 11, 12] the elements on a deep debate on the role of mean mass velocity and mean volume velocity in fluid mechanics.

1.2 A hierarchy of models

Instead of working with (3), it can be convenient to consider instead a solenoidal velocity field. From now on, we set

$$v = u + \kappa\nabla_x \ln(\rho).$$

Then (1) becomes a convection–diffusion PDE

$$\partial_t\rho + \nabla_x \cdot (v\rho) = \kappa\Delta_x\rho. \tag{6}$$

For the momentum equation (2), we start by writing it in non conservative form

$$\rho\big(\partial_t u + (u\cdot\nabla_x)u\big) + \nabla_x p = \rho g + \mathrm{Div}_x\big(2\mu\mathbb{D}(u)\big).$$

Next, we observe that

$$\begin{array}{rcl}\rho\partial_t u &=& \rho\partial_t v - \kappa\rho\partial_t\nabla_x\ln(\rho)\\ &=& \rho\partial_t v + \kappa\Big(\nabla_x(v\cdot\nabla_x\rho) - \dfrac{\nabla_x\rho}{\rho}v\cdot\nabla_x\rho\Big) - \kappa^2\Big(\nabla_x\Delta_x\rho - \dfrac{\nabla_x\rho}{\rho}\Delta_x\rho\Big),\end{array}$$

while

$$\mathrm{Div}_x\big(2\mu\mathbb{D}(u)\big) = \mathrm{Div}_x\big(2\mu\mathbb{D}(v)\big) - \kappa\mathrm{Div}_x\big(2\mu D_x^2\ln(\rho)\big)$$

where, for a scalar function $h : (t,x)\in(0,T)\times\mathbb{R}^N\mapsto h(t,x)\in\mathbb{R}$, we denote by $D_x^2 h$ the hessian matrix with components $\partial_{x_i}\partial_{x_j}h(t,x)$, and

$$\rho(u\cdot\nabla_x)u = \rho(v\cdot\nabla_x)v - \kappa\Big((\nabla_x\rho\cdot\nabla_x)v + \rho(v\cdot\nabla_x)\frac{\nabla_x\rho}{\rho}\Big) + \kappa^2(\nabla_x\rho\cdot\nabla_x)\frac{\nabla_x\rho}{\rho}.$$

Furthermore, we remark that

$$\nabla_x(v\cdot\nabla_x\rho) - \frac{\nabla_x\rho}{\rho}v\cdot\nabla_x\rho - \rho(v\cdot\nabla_x)\frac{\nabla_x\rho}{\rho} = \nabla_x v^T\nabla_x\rho.$$

Therefore we arrive at

$$\begin{array}{rcl}\rho\big(\partial_t v + (v\cdot\nabla_x)v\big) + \nabla_x p &=& \rho g + \mathrm{Div}_x(2\mu\mathbb{D}(v))\\ && +\kappa(\nabla_x v - \nabla_x v^T)\nabla_x\rho\\ && +\kappa^2\Big(\nabla_x\Delta_x\rho - \mathrm{Div}_x\Big(\dfrac{\nabla_x\rho\otimes\nabla_x\rho}{\rho}\Big)\Big)\\ && -\kappa\mathrm{Div}_x\big(2\mu D_x^2\ln(\rho)\big).\end{array}\tag{7}$$

The system (6)–(7) completed by the condition $\nabla_x\cdot v = 0$ is equivalent to (1)–(3). The advantage relies on the fact that we are dealing with a solenoidal velocity, but we have simplified the constraint at the price of introducing high order terms in the mass and momentum balance laws. For physical arguments favoring this formulation, we refer the reader to [9, 10, 12].

In the Appendix, we propose a derivation of Kazhikhov–Smagulov-like systems from a particulate-flow description: the dilute phase is described by means of its particle distribution function and the interaction with the carrier fluid is driven by drag forces. We discuss asymptotic regimes that allow us to identify limiting hydrodynamic equations. Let us now detail various manipulations and simplifications that can be performed on the model (6)–(7).

a) When the viscosity μ is constant, the last term in (7) is a gradient: $\kappa\mathrm{Div}_x\big(2\mu D_x^2\ln(\rho)\big) = 2\kappa\mu\nabla_x\Delta_x\ln(\rho)$ which can be incorporated in the pressure, like the term $\kappa^2\nabla_x\Delta_x\rho$. This is the situation treated in [36].

b) A more relevant case consists in assuming that μ is an affine function of ρ. It arises in particular when using the formula proposed in [26] for the effective viscosity of suspensions. According to [26], we have

$$\mu(\rho) = \mu_\star\Big(1 + \frac{N+2}{2}\phi\Big) = \mu_\star\Big(1 - \frac{N+2}{2}\frac{\bar\rho_f}{\bar\rho_d - \bar\rho_f} + \frac{N+2}{2(\bar\rho_d - \bar\rho_f)}\rho\Big) = \bar\mu + \tilde\mu\rho \tag{8}$$

with $\mu_\star$ the standard viscosity of the fluid, and N the space dimension. Like in a), the contribution in the last term of (7) associated to $\bar\mu$ can be incorporated in the pressure. The perturbation reads

$$2\tilde\mu \mathrm{Div}_x\big(\rho D_x^2 \ln(\rho)\big) = 2\tilde\mu\Big(\nabla_x\Delta_x\rho - \mathrm{Div}_x\Big(\frac{\nabla_x\rho\otimes\nabla_x\rho}{\rho}\Big)\Big).$$

The first term in the right hand side can disappear in the pressure gradient. With this assumption on μ, which appears in [24], (7) can be recast as

$$\begin{array}{rcl} \rho\big(\partial_t v + (v\cdot\nabla_x)v\big) + \nabla_x p & = & \rho g + \mathrm{Div}_x(2\mu(\rho)\mathbb{D}(v)) \\ & & +\kappa(\nabla_x v - \nabla_x v^T)\nabla_x\rho \\ & & +\kappa(\kappa - 2\tilde\mu)\mathrm{Div}_x\Big(\dfrac{\nabla_x\rho\otimes\nabla_x\rho}{\rho}\Big). \end{array} \tag{9}$$

c) The Kazhikhov-Smagulov model [47] is obtained by neglecting the last term in the right hand side of (9), which contains the higher nonlinearities and derivatives with respect to ρ, leading to :

$$\left\{\begin{array}{rcl} \partial_t\rho + \nabla_x\cdot(\rho v) & = & \kappa\Delta_x\rho, \\ \rho\big(\partial_t v + (v\cdot\nabla_x)v\big) + \nabla_x p & = & \rho g + \mathrm{Div}_x(2\mu(\rho)\mathbb{D}(v)) + \kappa(\nabla_x v - \nabla_x v^T)\nabla_x\rho, \\ \nabla_x\cdot v & = & 0, \end{array}\right. \tag{10}$$

This can be motivated by assuming $0 < \kappa \ll 1$ and $0 < \tilde\mu \ll 1$ (or $\tilde\mu = 0$ as in [36, 47]). The later makes sense with Einstein's formula (8) in the regime $\bar\rho_d/\bar\rho_f \gg 1$. The Kazhikhov-Smagulov system is analyzed in [47] and [5, Chap. 3, Sect. 4, sp. Theorem 4.1] for the case where μ is constant: assuming $\kappa < 4\frac{\mu}{\bar\rho_f - \bar\rho_d}$, where $0 < \bar\rho_f, \bar\rho_d < \infty$ stand for the extreme values of the initial density, the global existence (and uniqueness in dimension 2) of a weak solution is established. For the full model (6)–(7), local existence of solutions is shown in [6, 64], as well as global results for small data [6] or assuming a smallness condition on the ratio κ/μ [65]. Instead of using asymptotic arguments, ref. [24] gets rid of the last term in (9) by postulating a ad hoc relation between the coefficient κ and $\tilde\mu$, namely assuming $\kappa = 2\tilde\mu$. Not only this assumption simplifies the model, but it also leads to a remarkable balance law for the energy of the system, see [24, Section 2.2]. The mathematical analysis of this specific case is due to [13, 50, 49].

d) A further simplification arises by considering the viscosity μ constant and pushing forward the asymptotic regime in c). We get rid of all $\mathscr{O}(\kappa)$ terms, but not in the mass conservation.

We obtain in this way the Graffi model [42]

$$\left\{\begin{array}{rcl} \partial_t\rho + \nabla_x\cdot(\rho v) & = & \kappa\Delta_x\rho, \\ \rho\big(\partial_t v + (v\cdot\nabla_x)v\big) + \nabla_x p & = & \rho g + 2\bar{\mu}\mathrm{Div}_x\big(\mathbb{D}(v)\big), \\ \nabla_x\cdot v & = & 0. \end{array}\right. \tag{11}$$

A derivation of (11) from (6) and (9), with the divergence free constraint, is proposed in [36] in the regime of small Graffi numbers $\mathscr{G} = \frac{\bar{\mu}\kappa}{g\bar{\rho}_f \mathrm{L}^3} \ll 1$, with L a certain length of reference.

1.3 Application to powder–snow avalanches

Kazhikhov-Smagulov equations have been introduced in order to model pollution spread in atmospheric flows or contaminant spread in groundwater, with further analysis on the instability of certain layered configurations [36]. The model (10) has also been proposed to simulate the formation of powder-snow avalanches [24]. It also appeared in a slightly different form, with the dilute volume fraction as a privileged unknown, in [27, 30]. Powder-snow avalanches can be seen as a suspension cloud of snow particles, with a relatively dense core, surrounded by a suspension layer. During the motion along steep slopes, air is entrained in the flow. Thus, air and snow make a complex mixture. The physical characteristics of the flow make relevant to describe it like a single phase gravity flow [62, 29]. However the mixture is characterized by quite large density variations, the bulk density of the snow being a few tens that of the air. Accordingly Boussinesq's approximation in this context is highly questionable [27, 30, 56, 55], and using PDEs in the Kazhikhov-Smagulov hierarchy for the simulation of powder-snow avalanches looks a valuable attempt.

2 Numerical Simulations

This section is devoted to the numerical simulation of solutions arising from case c) above. It is convenient to work with dimensionless quantities. To this end, we introduce time and length scales of reference, denoted T and L, respectively. We set U = L/T as to be the velocity unit. We also need reference values for the mass density and the dynamic viscosity, $\bar{\rho} > 0$ and $\bar{\mu} > 0$ respectively. They define the kinematic viscosity $\bar{\nu} = \bar{\mu}/\bar{\rho}$. Accordingly, with the convention that starred quantities are dimensionless, we set

$$\begin{array}{ll} t = t_\star\,\mathrm{T}, & x = x_\star\,\mathrm{L}, \\ v(t,x) = \mathrm{U}\,v_\star(t_\star,x_\star), & \rho(t,x) = \bar{\rho}\,\rho_\star(t_\star,x_\star), \\ \mu(\rho) = 2\,\bar{\nu}\,\bar{\rho}\,\mu_\star(\rho_\star). & \end{array}$$

We finally define the unit vector pointing in the direction of the gravity field $g_\star$ by $g = \|g\|\,g_\star$. To make the notation less cluttered, we skip from now on all the stars subscripts, having in mind that, unless explicitly mentioned, all the variables are understood as dimensionless ones. Then, the dimensionless form of the system reads :

$$\left\{\begin{array}{llcl} (i) & \partial_t \rho + \nabla_x \cdot (\rho v) & = & \dfrac{1}{\mathrm{Re}\,\mathrm{Sc}}\Delta_x \rho, \\ (ii) & \rho\big(\partial_t v + (v\cdot\nabla_x)v\big) + \nabla_x p & = & \dfrac{1}{\mathrm{Fr}^2}\rho g + \dfrac{1}{\mathrm{Re}}\mathrm{Div}_x(\mu(\rho)\mathbb{D}(v)) \\ & & & +\dfrac{1}{\mathrm{Re}\,\mathrm{Sc}}(\nabla_x v - \nabla_x v^T)\nabla_x \rho, \\ (iii) & \nabla_x \cdot v & = & 0. \end{array}\right. \tag{12}$$

The physics is embodied into three dimensionless parameters: the Reynolds number Re, the Froude number Fr and the Schmidt number Sc:

$$\mathrm{Re} = \frac{\mathrm{U\,L}}{2\bar{\nu}}, \qquad \mathrm{Fr} = \frac{\mathrm{U}}{\sqrt{\|g\|\mathrm{L}}}, \qquad \mathrm{Sc} = \frac{2\,\bar{\nu}}{\kappa}. \tag{13}$$

The Reynolds number evaluates the strength of convection compared to viscous diffusion, the Froude number compares the strength of inertial and gravity forces, and the Schmidt number is the ratio of viscosity (velocity diffusivity) and mass diffusivity. Dealing with mixture flows, it is also relevant to introduce the so–called densimetric Froude number, which is defined by:

$$\mathrm{Fr}_d = \frac{\mathrm{U}}{\sqrt{\|g\|\mathrm{L}\,\dfrac{\Delta\rho}{\rho_d}}},$$

where $\Delta\rho = \bar{\rho}_f - \bar{\rho}_d$ is the difference between the extremal values of the density in the flow.

The equations are set on a bounded domain $\Omega \subset \mathbb{R}^N$ ($N = 2$ in the numerical experiments below). The definition of relevant boundary conditions that complete (12) is definitely a delicate modeling issue. All the simulations discussed below are performed by using the no-slip boundary condition for the velocity field and the Neumann boundary condition for the density

$$v\big|_{\partial\Omega} = 0, \qquad \nabla_x\rho\cdot\vec{n}\big|_{\partial\Omega} = 0, \tag{14}$$

with $\vec{n}$ the outward normal unit vector on $\partial\Omega$. As a matter of fact, (14) ensures that there is no mass influx, and the total mass is conserved by the system: $\frac{\mathrm{d}}{\mathrm{d}t}\int_\Omega \rho(t,x)\,\mathrm{d}x = 0$. These boundary conditions are equally used for the mathematical investigation of the problem in [5, 13, 44]. They also complete the system (12) for the simulations of avalanches in [24]. In [27, 30], the Neumann boundary condition is maintained for the density, but the no-slip condition is imposed on the mean mass velocity $u = v - \frac{1}{\mathrm{ReSc}}\nabla_x \ln(\rho)$. It also makes sense to impose a friction law, characterized by a coefficient $0 < \alpha < 1$, on the velocity

$$v\cdot\vec{n}\big|_{\partial\Omega} = 0, \qquad \big[(1-\alpha)v + \alpha\mathbb{D}(v)\vec{n}\big]\cdot\vec{t}\big|_{\partial\Omega} = 0,$$

with $\vec{t}$ the tangential vector at $\partial\Omega$, see [24], or its equivalent form on u, see [27, 30]. To decide whether the mean mass or the mean volume velocity enters into the no-slip boundary condition is an issue subject to debate. In [10] it is argued that the boundary condition should be

$$u\cdot\vec{n}\big|_{\partial\Omega} = 0, \qquad (\mathbb{I} - \vec{n}\otimes\vec{n})v\big|_{\partial\Omega} = 0.$$

2.1 Description of the scheme

Several numerical approaches are available for the numerical approximation of the solutions of (12). The simulations in [24] are realized with the open–source code `OpenFoam`; as far as we know the simulations are based on a second order upwind finite volume scheme, performed on a fixed Cartesian grid (but we are not aware of the technical details of the whole scheme). A dedicated code has been developed in [27, 29, 30]. It uses Finite Element discretizations, coupled to a characteristic method to treat the convection terms. The scheme is coupled to mesh refinement procedures, in order to follow the displacement of the avalanche front. Reference [44] is concerned with numerical analysis purposes only; the proposed Finite Element scheme is not implemented. The simulations of [55, 56, 58], based on a different system of PDEs, are done with the commercial code `Fluent`, which uses a Finite Element discretization on Cartesian grids.

In what follows, we propose a dedicated scheme for (12). The method is based on a hybrid finite volume/finite element strategy, which has been introduced in [16] for the resolution of the non homogeneous incompressible Navier-Stokes system[1]. The algorithm is based on a time splitting, and each equation is approached by a well–adapted method: we discretize the mass conservation equation (12)-(i) by using a Finite Volume scheme and the momentum equation 12)-(ii) coupled with the constraint (12)-(iii) is solved by using a Finite Element approximation. Two ingredients are crucial in the construction of the scheme:

- A relevant definition of footbridges between the two velocities discretizations (FE vs. FV) in order to make them compatible [16].
- Working with high order methods and unstructured meshes is a necessity; however, preserving the maximum principle in this framework needs the definition of suitable limiters. This issue is discussed in [14]; it is absolutely crucial to consider flows with high density contrasts and to follow fronts by a mesh refinement method.

Let us describe how we can adapt the scheme described in [14, 16] in order to explore numerically the system (12). From now on, we restrict the discussion to the two-dimensional framework. We consider a mesh of the computational domain made of triangles. We associate to this primal mesh the dual mesh obtained by joining the barycenters of the triangles to the midpoints of the edges, see Figure 1. The elements of this tessellation are the control volumes of the finite volume approximation: the discrete density ρ_C^n is intended to approximate the mean-value $\frac{1}{|C|}\int_C \rho(t^n, y)\,\mathrm{d}y$ of the physical density over the control volume C at time t^n. Note that the discrete densities are stored at the vertices of the primal mesh (Vertex-Based method). By contrast, the discrete velocity and pressure which define approximations of v and p are continuous on Ω and piecewise polynomials on the triangles of the primal mesh. Here, we shall use $\mathbb{P}_2$ and $\mathbb{P}_1$ approximations, respectively, but other choices such as $\mathbb{P}_1$-Bubble and $\mathbb{P}_1$ are possible.

Let $h > 0$ be a parameter characterizing the space discretization. At time t^n, we have at hand the discrete evaluations of the density ρ_h^n (defined by $\rho_h^n\big|_C = \rho_C^n$ for all control volumes C) and of the

---

[1] An Open-Source version of the code dealing with $2D$ Incompressible Navier-Stokes equations with non homogeneous density is available at the URL: `http://math.univ-lille1.fr/~simpaf/SITE-NS2DDV/home.html`

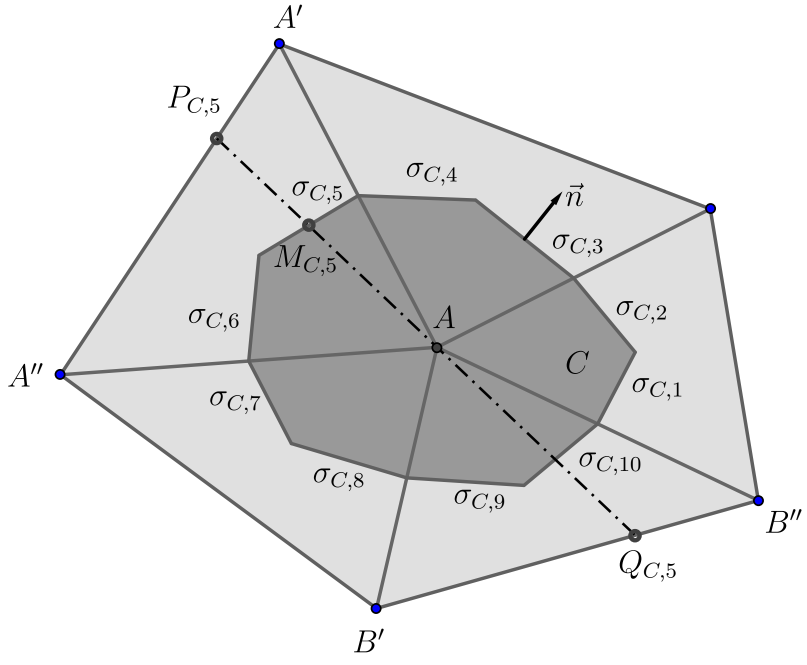

Figure 1: Primal and dual meshes.

velocity-pressure field (v_h^n, p_h^n). We update the unknowns according to a time-splitting approach. The scheme is constructed according to the following techniques:

1) Let us start by explaining how we proceed with the momentum equation (12)-(*ii*) with the constraint (12)-(*iii*); we postpone for a while the treatment of the mass conservation equation, and we assume that we have already computed ρ_h^{n+1}. We use the standard FE framework: we denote by Ω_h the computational domain which approaches the domain Ω. It is covered by triangles $T \in \mathscr{T}_h$. The approximations spaces are defined by

$$\begin{aligned} V_h &= \big\{ w_h \in C^0(\Omega_h),\ w_h\big|_T \in \mathbb{P}_2(T)\ \forall T \in \mathscr{T}_h,\ w_h\big|_{\partial\Omega_h} = 0 \big\}, \\ Q_h &= \big\{ q_h \in C^0(\Omega_h),\ q_h\big|_T \in \mathbb{P}_1(T)\ \forall T \in \mathscr{T}_h \big\}. \end{aligned}$$

Multiplying (12)-(*ii*) and (12)-(*iii*) by w_h and q_h spanning the basis of V_h and Q_h respectively, we obtain the following system for updating the velocity and pressure

$$\begin{aligned} &\frac{1}{\Delta t}\int_{\Omega_h} \widetilde{\rho_h^{n+1}}\left(v_h^{n+1} - v_h^n\right)\cdot w_h\,\mathrm{d}x + \int_{\Omega_h} \widetilde{\rho_h^{n+1}}(\overline{v}_h^{n+1}\cdot\nabla_x v_h^{n+1}) w_h\,\mathrm{d}x \\ &\qquad -\frac{1}{\mathrm{Re}}\int_{\Omega_h} \mu(\widetilde{\rho_h^{n+1}})\mathbb{D}(v_h^{n+1}) : \nabla_x w_h\,\mathrm{d}x - \int_{\Omega_h} p_h^{n+1}\nabla_x\cdot w_h\,\mathrm{d}x \\ &\qquad\qquad = \frac{1}{\mathrm{Fr}^2}\int_{\Omega_h} \widetilde{\rho_h^{n+1}} g\cdot w_h\,\mathrm{d}x + \frac{1}{\mathrm{ReSc}}\int_{\Omega_h} (\nabla_x v_h^{n+1} - (\nabla_x v_h^{n+1})^T)\nabla_x \widetilde{\rho_h^{n+1}}\cdot w_h\,\mathrm{d}x, \\ &\int_{\Omega_h} \nabla_x\cdot v_h^{n+1}\ q_h\,\mathrm{d}x = 0. \end{aligned} \tag{15}$$

When the Reynolds number Re becomes large and/or the Schmidt number Sc becomes small, an appropriate upwinding process on the convective term has to be designed to ensure the stability of the scheme (15); for instance SUPG methods can be used in such cases. On the same token we can also mention the recent attempt [40] which proposes a numerical treatment fully in the FV framework of the Incompressible Navier-Stokes equation, with a construction that imposes a certain consistency on the convective mass and momentum fluxes. Nevertheless, in our simulations Re is not so large and Sc is of order 1 (see also [24, 54, 55, 56]), and we did not experience any stability difficulty with the proposed centered scheme. In the integrals, we need to define the ("FE approximation" of the) density $\widetilde{\rho_h^{n+1}}$, from ρ_h^{n+1}, which is supposed to be constant on the control volumes. But, given a triangle T we can use the densities stored on the three vertices to construct a $\mathbb{P}_1$ interpolation: it defines $\widetilde{\rho_h^{n+1}}$. In turn, $\nabla_x\widetilde{\rho_h^{n+1}}$ is well-defined as a $\mathbb{P}_0$ function on the triangle. It allows us to treat the new coupling terms. With this definition, and using an extrapolation formula in order to approximate the velocity $\overline{v}_h^{n+1}$ at time $(t^n + \Delta t)$, the implicit system can be solved by using standard methods of incompressible numerical fluid mechanics. The integrals in (15) are evaluated by using an approximated integration method over the cells, which is exact for polynomials of degree $k \leq 6$. We do not use any mass-lumping process. Also, we recognize with the diffusion and pressure terms the classical form of a saddle point problem which can be written in matrix form

$$\begin{pmatrix} A & B^T \\ B & 0 \end{pmatrix} \begin{pmatrix} v_h^{n+1} \\ p_h^{n+1} \end{pmatrix} = \begin{pmatrix} f_h \\ 0 \end{pmatrix}.$$

Our simulation is based on the Uzawa algorithm, but projection methods (see [43] for an overview) can be used as well. Note however that the equivalent diffusion equation for the pressure has variable coefficients due to density inhomogeneities (roughly speaking, the operator typically reads $\nabla_x \cdot (\frac{1}{\rho}\nabla_x p)$). When the density ratio becomes high it might lead to intricate conditioning difficulties, see [15]. Of course, variations of this formula can be proposed, either by treating less terms fully implicitely (e. g. in the source and in the convection) or by using a more elaborate time discretization (see further comments below).

2) We turn to the treatment of the mass conservation. Updating the density ρ_h^{n+1} relies on integrating (12)-(i) over $[t^n, t^n + \Delta t] \times C$

$$\begin{aligned} \int_C \rho(t^n + \Delta t, x)\,\mathrm{d}x - \int_C \rho(t^n, x)\,\mathrm{d}x \\ = -\int_{t^n}^{t^n+\Delta t} \int_{\partial C} \rho(t,x) v(t,x) \cdot \vec{n}\,\mathrm{d}\sigma(x)\,\mathrm{d}t \\ + \frac{1}{\mathrm{ReSc}} \int_{t^n}^{t^n+\Delta t} \int_{\partial C} \nabla_x \rho(t,x) \cdot \vec{n}\,\mathrm{d}\sigma(x)\,\mathrm{d}t. \end{aligned}$$

Here and below, $\vec{n}$ stands for the outward normal unit vector on ∂C. The left hand side is approached by $(\rho_C^{n+1} - \rho_C^n)\,|C|$ and we need to define relevant convection and diffusion numerical fluxes. The interface ∂C is the reunion of a finite number of segments: $\partial C =$

$\bigcup_j \sigma_{C,j}$, see Figure 1. Hence,

$$\begin{aligned}&\int_{t^n}^{t^n+\Delta t}\int_{\partial C}\rho(t,x)v(t,x)\cdot\vec{n}\,\mathrm{d}\sigma(x)\,\mathrm{d}t\\&=\sum_j\int_{t^n}^{t^n+\Delta t}\int_{\sigma_{C,j}}\rho(t,x)v(t,x)\cdot\vec{n}\,\mathrm{d}\sigma(x)\,\mathrm{d}t \text{ is approached by } \Delta t\sum_j|\sigma_{C,j}|\rho_j^n v_j^n\cdot\vec{n},\end{aligned}$$

where the interface values ρ_j^n, v_j^n should be defined from the available numerical unknowns. Since v_h^n is piecewise $\mathbb{P}_2$, it might be tempting just to evaluate it directly on the segment $\sigma_{C,j}$ in order to get $v_j^n\cdot\vec{n}$ (say for instance v_j^n is the value of v_h^n at the midpoint of the segment $\sigma_{C,j}$). In [16] we boil down a different definition of the normal velocity $v_j^n\cdot\vec{n}$. The argument states as follows: since the velocity field is divergence free, an homogeneous density should remain homogeneous. The naive construction does not fulfill this requirement. Indeed, for the FV viewpoint a solenoidal velocity field satisfies

$$\int_{\partial C} v\cdot\vec{n}\,\mathrm{d}\sigma=\sum_j\int_{\sigma_{C,j}} v\cdot\vec{n}\,\mathrm{d}\sigma=0,$$

which becomes at the discrete level

$$\sum_j|\sigma_{C,j}|v_j^n\cdot\vec{n}=0. \tag{16}$$

But, the velocity field v_h^n produced by the FE step is only required to satisfy

$$\int_{\Omega_h}\nabla_x\cdot v_h^n\ q_h\,\mathrm{d}x=0 \tag{17}$$

for any basis element q_h of the FE space Q_h. Therefore we proceed as follows. Let us denote by A the vertex which is the center of the control volume C. We assume it is the common vertex of K triangles of the primal mesh. Writing (17) with q_h the basis function associated to A, the remarkable fact is that we obtain an expression which involves only the values of v_h^n at the midpoints of the edges of these K triangles having A as a common vertex. When $\sigma_{C,j}$ lies in a triangle T, we write v_j^n as a convex combination of these evaluations of v_h^n at the midpoints of the edges of T. Going back to (16) identifies the coefficients of this combination: it coincides with a linear 2D interpolation at the barycenter from velocities known at these nodes. We refer the reader to [16] for further details.

3) We are left with the task of defining ρ_j^n. Of course, we can simply use upwinding according to the sign of $v_j^n\cdot\vec{n}$, but the corresponding scheme has poor accuracy. We propose a MUSCL method with multislope limiters (see Figure 1). The interface value on $\sigma_{C,j}$ of the density is defined by

$$\rho_j^n=\rho_C^n+p_{C,j}|AM_{C,j}|$$

where $M_{C,j}$ is the midpoint of the segment $\sigma_{C,j}$. The increment $p_{C,j}$ is defined through the following procedure. We remind that $\sigma_{C,j}$ lies in a certain triangle T of the primal mesh, and, of course, A is one of the vertices of T. We draw the line $AM_{C,j}$. It intersects the edge of T opposite to A in a point that we denote $P_{C,j}$. The line also intersects the edge of another triangle S having A among its vertices; we denote by $Q_{C,j}$ the intersection point. It turns out that $AP_{C,j}$ (resp. $AQ_{C,j}$) can be written as a convex combination of AA' and AA'' with $T = (A, A', A'')$ (resp. AB' and AB'' with $S = (A, B', B'')$). Then, we define $\rho(P_{C,j})$ (resp. $\rho(Q_{C,j})$) as the convex combination with the same weight of $\rho_C = \rho(A)$, $\rho(A')$ and $\rho(A'')$ (resp. $\rho_C = \rho(A)$, $\rho(B')$ and $\rho(B'')$): namely if $AP_{C,j} = \lambda AA' + (1 - \lambda)AA''$, then we set

$$\rho(P_{C,j}) = \rho(A) + \lambda(\rho(A') - \rho(A)) + (1 - \lambda)(\rho(A'') - \rho(A))$$

(and a similar formula for $\rho(Q_{C,j})$). Next, we introduce the quantities

$$p^{\mathrm{up}}_{C,j} = \frac{\rho(A) - \rho(Q_{C,j})}{|AQ_{C,j}|}, \qquad p^{\mathrm{down}}_{C,j} = \frac{\rho(P_{C,j}) - \rho(A)}{|AP_{C,j}|}, \qquad r_{C,j} = \frac{p^{\mathrm{down}}_{C,j}}{p^{\mathrm{up}}_{C,j}}.$$

Finally, we set

$$p_{C,j} = p^{\mathrm{up}}_{C,j} \times \Psi(r_{C,j})$$

where Ψ is a limiter function which has to satisfy some specific properties (namely, the "τ-limiter" property). We can use for instance the MinMod limiter, or a modified Van Leer limiter. This scheme is introduced in [14] where the L^∞ stability is established under a suitable CFL condition. Of course the definition of the CFL number relies on certain geometric quantities, but the scheme can be shown to be stable without geometric constraint on the mesh, by contrast to the situation known for the Cell-Center framework [18]. We also refer the reader to [44] for recent progress on these questions, including in the 3-dimensional framework.

4) For the diffusion fluxes, we interpret again the density as a piecewise $\mathbb{P}_1$ function on each triangle of the primal mesh. It allows to properly define an approximation of $\frac{1}{\mathrm{ReSc}} \int_{\partial C} \nabla_x \rho \cdot \vec{n}\, \mathrm{d}\sigma$ on each component of ∂C. This idea is reminiscent of the so–called FVE method for the discretization of diffusion equations [21, 35, 31, 33], and [32, Section 3.4.3]. Diffusion is treated implicitly so that we can expect it does not deteriorate the stability condition. Note that the preservation of the discrete maximum principle by such finite volume methods for convection-diffusion equation is a delicate question. It might induce some restrictions on the meshes like in [35], or require a more refined definition, possibly non-linear, of the diffusion fluxes. The use of such elaborate schemes is beyond the scope of this work; a detailed exposition of the state of the art can be found in [23] and the references therein. In our numerical simulations, we did not experience loss of positivity that could be due to the treatment of the diffusion term.

5) Finally, for the simulation we use a more involved time integrator, in order to preserve the global second-order accuracy both in time and space. The time splitting is treated with the Strang algorithm. In the momentum equation, the time discretization is based on the BDF second order scheme, and the value of $\bar{v}_h^{n+1}$ arising in (15) is given by an extrapolation formula of order 2. In the mass conservation, the time discretization is based on an Adam-Bashforth scheme of order two for the transport term and the Crank-Nicolson scheme for the diffusive term, which formally leads to second-order consistency.

Remark 1 *Different procedures can be used to construct the dual mesh of the triangulation. For instance, we can use the so–called dual Voronoi tesselation, which is obtained from the primal triangulation by joining the centers of the circumcircles (in general not identical with the barycenters of the triangles), or we can simply join the barycenters. However, proving the L^∞ stability of the scheme requires further geometric constraints and the scheme might become less accurate, see [14, Section 2.3]. This remark motivates the construction presented above.*

2.2 Validation of the Scheme: Comparison to an Exact Solution

To start with, we evaluate the ability of the scheme to recover a smooth analytical solution and we check the corresponding rates of convergence. We pay attention to the robustness of the scheme with respect to mesh variation and we verify that the new coupling terms do not alter the accuracy compared to the incompressible case. Here, the computational domain is the square $\Omega = [-1, 1]^2$. The explicit solution we wish to capture is given by

$$\left\{ \begin{array}{rcl} \rho_{\text{ex}}(x,y,t) &=& 2 + \cos x \, \sin y \, \sin t, \\ v_{\text{ex}}(x,y,t) &=& (-4y(x^2-1)^2(y^2-1)\, ,\, 4x(y^2-1)^2(x^2-1))^T, \\ p_{\text{ex}}(x,y,t) &=& \sin x \, \sin y \sin t. \end{array} \right. \tag{18}$$

The set of equations (12) is solved on the time interval $0 \le t \le 0.2$, using $\text{Re} = 1$ and without any gravity field ($g = 0$). Like in [24], we suppose that the viscosity depends affinely on the density by setting $\mu(\rho) = 1 + \rho/2$. The appropriate source terms $f^{(1)}$ and $f^{(2)}$ are added in the right-hand side of the two first equations in (12), so that (18) is indeed a solution.

We work with unstructured meshes generated by the `BAMG` software. This software can create a mesh from a given geometry or adapt a mesh from a background mesh using a variable metric based on the density. We point out that, in general, the produced meshes are not regular in the sense of Delaunay. The time step Δt is proportional to $h_{\min}$, the length of the smallest convex radius in the mesh (see Table 1), so that the CFL stability criterion is always ensured. The maximal errors in ρ, v and p are recorded during the time interval and given as a function of $h_{\max}$, the length of the largest edge in the mesh. They are evaluated in the $L^1(\Omega)$ and $L^2(\Omega)$ norm for the density (namely $\|\rho_{\text{ex}} - \rho_h\|_{L^1(\Omega)}$ and $\|\rho_{\text{ex}} - \rho_h\|_{L^2(\Omega)}$), and in the $L^2(\Omega)$ norm for the velocity and the pressure (namely $\|v_{\text{ex}} - v_h\|_{L^2(\Omega))}$ and $\|p_{\text{ex}} - p_h\|_{L^2(\Omega)}$).

Firstly, we check the influence of the new coupling terms. We consider (12) with $\text{Sc} = \infty$: we get rid of the right-hand-side in (12)-(i) and we get rid of the last term of the right-hand-side in (12)-(ii), and the system degenerates into the incompressible variable density Navier-Stokes system. As we can see in Figure 2(a), the convergence is ensured, and Table 2 shows that the convergence rates computed from the results obtained on the two finest grids are similar to those reported in [14, Section 4.1] with similar unstructured meshes. Next, we consider (12) with $\text{Sc} = 1$. As we can see in Figure 2(b), the convergence is also ensured. Table 2 shows that the corresponding convergence rates are even better than for the first test.

Secondly, we consider deformed meshes obtained applying a random translation proportional to h_{min} to each internal node of the grids generated by the BAMG software. We plot in Figure 3 the coarsest meshes obtained using BAMG and applying such a random small translation. This

Mesh level	1	2	3	4	5	6
h_{max}	0.25	0.125	0.0625	0.03125	0.015625	0.078125
h_{min}	0.0686	0.0353	0.0166	0.00777	0.00398	0.001649

Table 1: h_{max} and h_{min} values on non structured meshes.

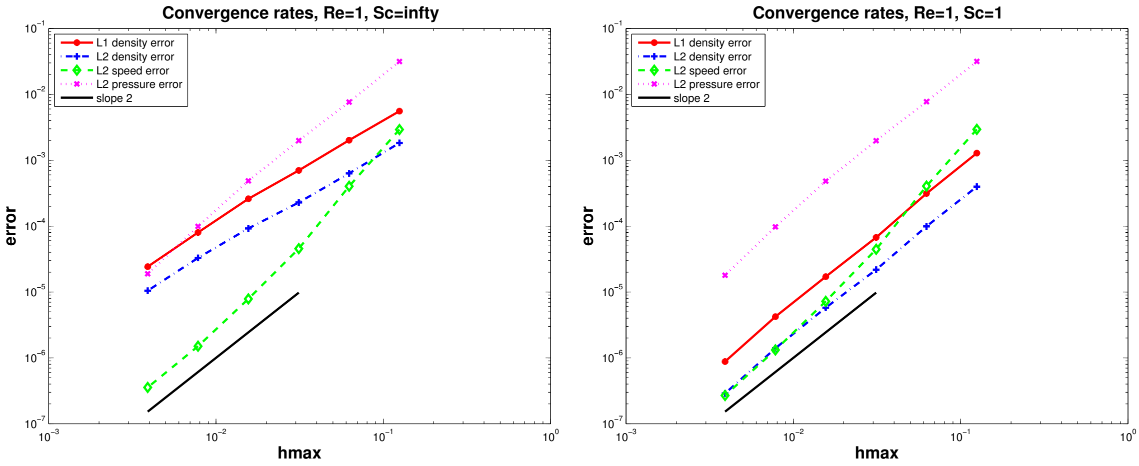

(a) : $Sc = \infty$ (b) : $Sc = 1.0$

Figure 2: Convergence rates of the numerical scheme for the analytical solution with regular meshes.

perturbation is intended to mimic mesh deformations that appear when some adaptive procedures are applied. We perform the same two tests, Sc $= \infty$ and Sc $= 1$, on the deformed meshes: we can see in Figure 4 ((a) for Sc $= \infty$ and (b) for Sc $= 1$) that the convergence is confirmed. Table 2 gives the corresponding convergence rates which remain second-order accurate, except for the density in the case Sc $= \infty$, where a lower rate of convergence is achieved, remaining nevertheless very satisfactory and close to the case of non deformed meshes.

Hence, we conclude from these experiments that the treatment of the new terms $\frac{1}{\text{ReSc}}\Delta_x \rho$ in (12)-(i) and $\frac{1}{\text{ReSc}}(\nabla_x v - \nabla_x v^T)\nabla_x \rho$ in (12)-(ii), as well as small random translations of the nodes, do not alter significantly the accuracy of the scheme.

	$BAMG$		$BAMG + random$	
	$Sc = \infty$	$Sc = 1.0$	$Sc = \infty$	$Sc = 1.0$
Convergence rate in $\|\rho_{\text{ex}} - \rho_h\|_{L^1(\Omega)}$	1.72	2.26	1.58	2.17
Convergence rate in $\|\rho_{\text{ex}} - \rho_h\|_{L^2(\Omega)}$	1.65	2.27	1.37	2.19
Convergence rate in $\|v_{\text{ex}} - v_h\|_{L^2(\Omega)}$	2.08	2.29	2.08	2.34
Convergence rate in $\|p_{\text{ex}} - p_h\|_{L^2(\Omega)}$	2.39	2.44	2.15	2.23

Table 2: Convergence rates for the exact solution.

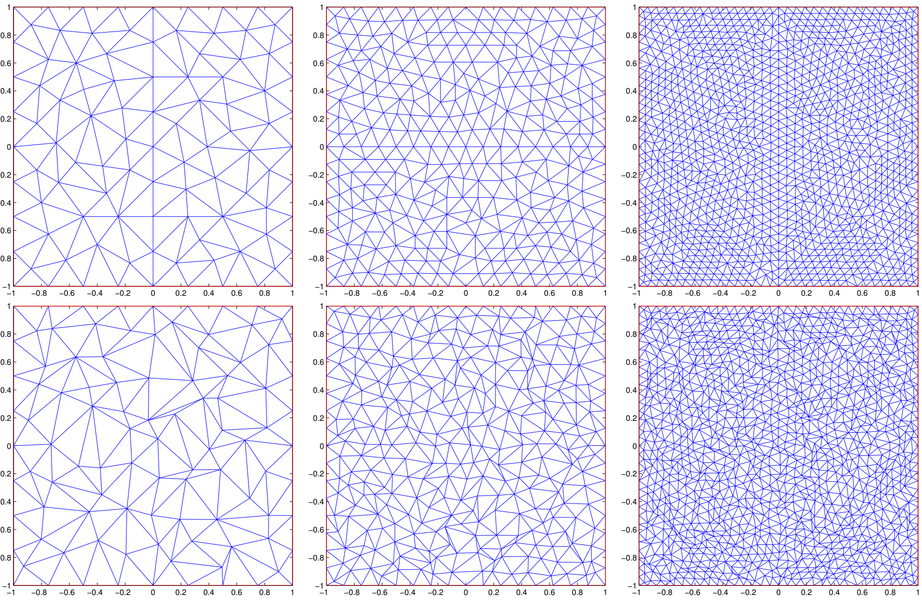

Figure 3: First line: regular meshes generated by the BAMG software, with mesh levels 1, 2, 3. Second line: deformed meshes obtained applying a random perturbation $(x_i, y_i) + h_{min} * rand()$.

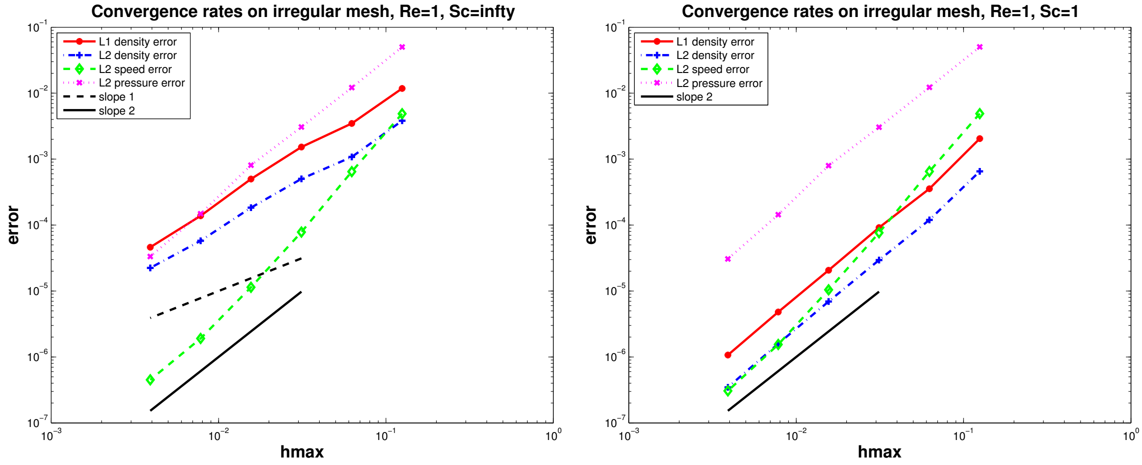

(a) : $Sc = \infty$ (b) : $Sc = 1.0$

Figure 4: Convergence rates of the numerical scheme for the analytical solution with deformed meshes.

2.3 Simulation of an Avalanche Interacting With an Obstacle

2.3.1 Resolution in Physical Variables

We are now interested in the simulation of the interaction of an avalanche with an obstacle, a case addressed in [24]. In order to have a direct comparison we go back to the physical quantities: in this subsection we deal with dimensional variables. Namely, we consider the system (10) completed by (14): homogeneous Dirichlet boundary condition on the velocity filed, and homogeneous Neumann boundary condition on the density field. A heavy fluid flows under the effect of the gravity force along an inclined channel and interacts with an obstacle. This kind of simulation is motivated by the dimensioning of protection devices, see also [55, 56]. We refer the reader to the schematic representation in Figure 5. The parameters are specified in Table 3. Initially, the heavy fluid $\bar{\rho}_f$, located in the rectangle $[2l_0/3,\ h_0/3]$, is surrounded by a fluid with intermediate density $\tilde{\rho} = \bar{\rho}_d + 0.4\,(\bar{\rho}_f - \bar{\rho}_d)$. This configuration is intended to roughly mimic the observed layers in actual avalanches, with dense snow on the ground, topped by a fluidized bed that might degenerate to an aerosol flow.

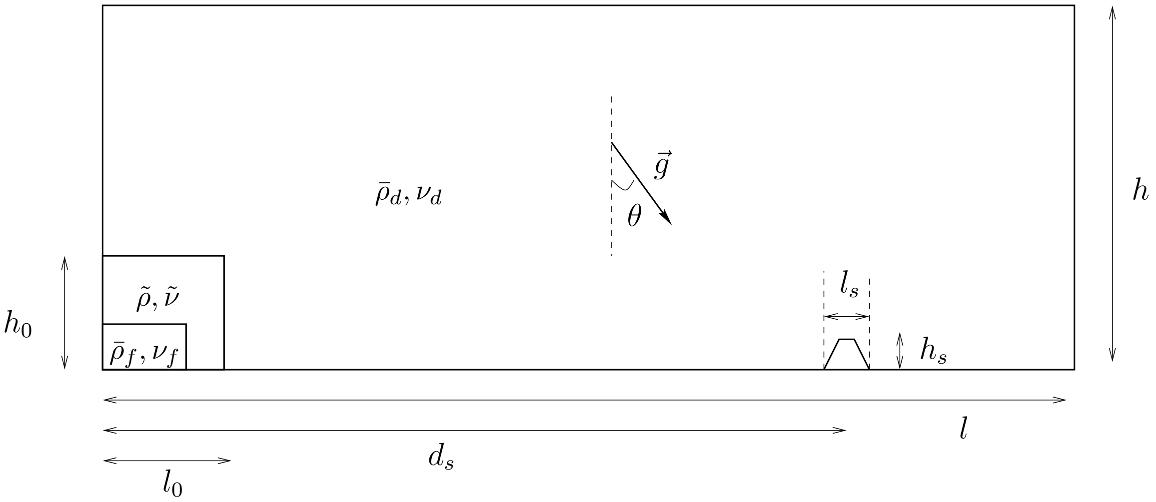

Figure 5: Domain and initial data configurations.

We take in (10) the following parameters :

$$\kappa = 2\,\overline{\nu} \ \text{ with } \ \overline{\nu} = \frac{\nu_f \bar{\rho}_f - \nu_d \bar{\rho}_d}{\bar{\rho}_f - \bar{\rho}_d}, \ \text{ and } \mu = \overline{\nu}\,\rho. \tag{19}$$

Concerning the numerical parameters, the mesh is made of an unstructured tessellation of triangles, and the smallest convex radius (resp. the smallest edge) is about $h_{\min} \approx 7 \times 10^{-4}\,m$ (resp. $2 \times 10^{-3}\,m$). The mesh evolves dynamically in order to follow the displacement of the front of the avalanche with finer structures in the regions of large density gradients, using an adaptive mesh refinement strategy, based on the `BAMG` software. The number of triangles in the mesh increases up to 15 000 at the end of the simulation. The computational time step is set to $\Delta t = 10^{-3}\,s$. We have performed a series of simulations by making both the time step and the mesh size vary in order to

Gravity acceleration $\|g\|$, $m\,s^{-2}$	9.8
Slope of the inclined channel θ, °	32
Heavy fluid density $\bar{\rho}_f$, $kg\,m^{-3}$	20
Light fluid density $\bar{\rho}_d$, $kg\,m^{-3}$	1
Heavy fluid kinematic viscosity ν_f, $m^2\,s^{-1}$	$4,8.10^{-4}$
Light fluid kinematic viscosity ν_d, $m^2\,s^{-1}$	$1,0.10^{-4}$
Domain height h, m	0.8
Domain length l, m	2.7
Initial avalanche height h_0, m	0.3
Initial avalanche length l_0, m	0.3
Obstacle height h_s, m	0.06
Obstacle thickness l_s, m	0.04
Obstacle distance d_s, m	1.92

Table 3: Avalanche simulation : physical parameters.

guaranty that the convergence grid is reached. Results are reported in Figure 6 where the isovalues of the density and the magnitude of the velocity are displayed.

We can observe a qualitatively satisfactory correspondence between the snapshots presented in Figure 6 and Figures 5 to 7 of [24], corresponding to the same physical data (the time scale has been erroneously reported in Figures 5 to 9 of [24]; it needs to be corrected to fit with the data: roughly speaking the reported time should be divided by 60). At the very first times of the simulation, we recognize the emergence of a classical elliptic front. Then during the sliding regime we can already observe the formation of Kelvin-Helmholtz instabilities, with a large vortex that takes place behind the head of the flow, above a zone of light density where the fluid is dragged by the avalanche. Finally, the interaction with the obstacle generates a jet directed upward, with the formation of the mushroom shape corresponding to a classical Rayleigh-Taylor instability. As it has been already pointed out elsewhere, both from numerical or experimental studies [24, 27, 30, 45, 54, 55, 56], the maximal velocity within the avalanche exceeds the front speed by 30% to 40%.

2.3.2 Resolution in Dimensionless Variables

We perform now the same simulation than the one in subsection 2.3.1, but working with the dimensionless system. This is important to check whether the choice of the reference units is relevant. To this end, we use as characteristic units the height of the avalanche $\mathrm{L} = h_0 = 0.3\,m$, the gravity acceleration $\|g\| = 9.8\,m\,s^{-2}$ and the density contrast defined by the value $\Delta\rho/\bar{\rho}_d = (\bar{\rho}_f - \bar{\rho}_d)/\bar{\rho}_d$. Following [30], the densimetric Froude number is fixed to be equal to one, which gives us the velocity scale $\mathrm{U} = \sqrt{L\|g\|\Delta\rho/\bar{\rho}_d} = 7.47\,m\,s^{-1}$. Accordingly, we obtain from (13) and the choices made in (19) the values :

$$\mathrm{Re} = 2242, \ \mathrm{Fr} = 4.3589, \ \mathrm{Sc} = 1.0.$$

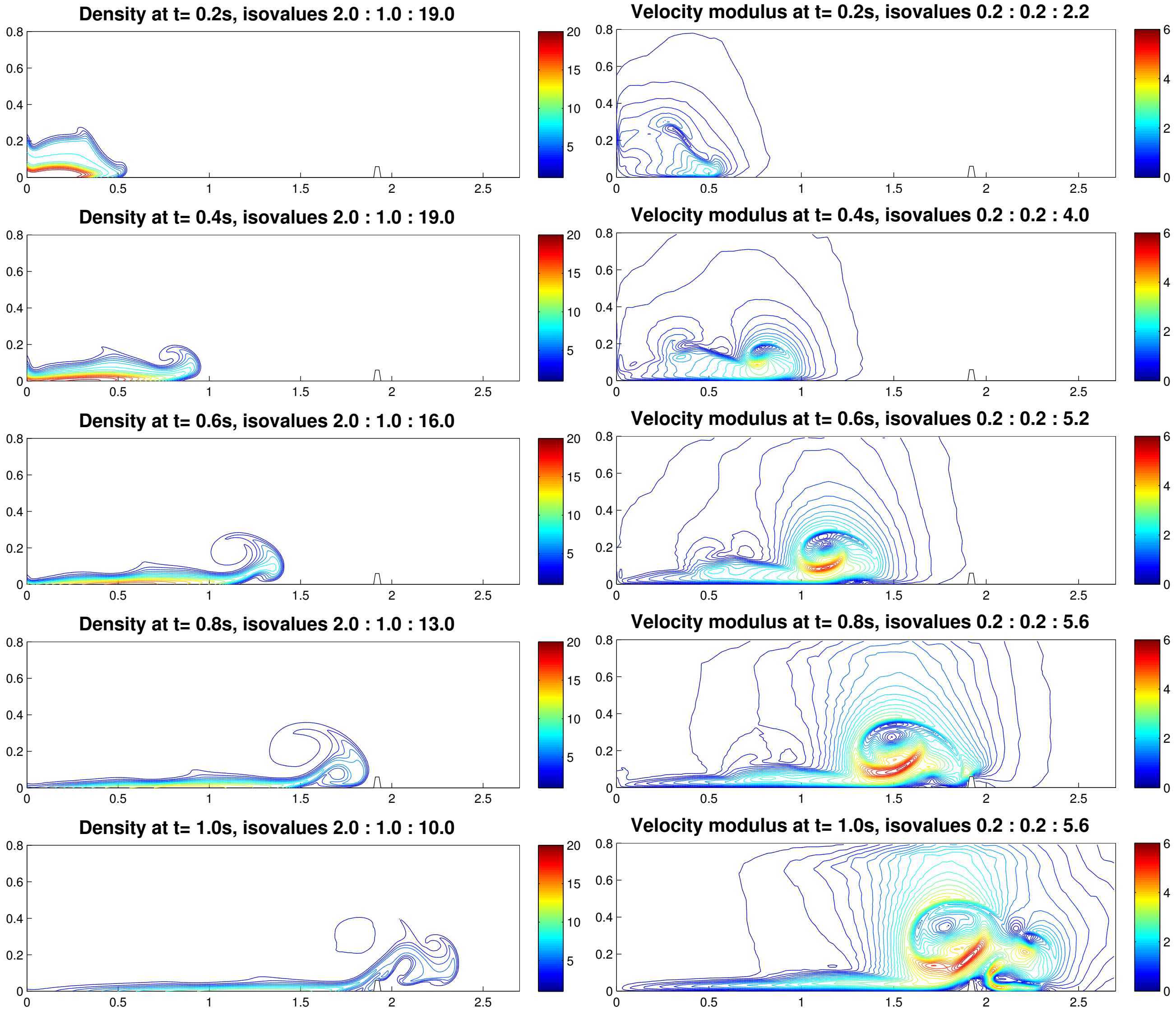

Density at t= 0.2s, isovalues 2.0 : 1.0 : 19.0

Velocity modulus at t= 0.2s, isovalues 0.2 : 0.2 : 2.2

Density at t= 0.4s, isovalues 2.0 : 1.0 : 19.0

Velocity modulus at t= 0.4s, isovalues 0.2 : 0.2 : 4.0

Density at t= 0.6s, isovalues 2.0 : 1.0 : 16.0

Velocity modulus at t= 0.6s, isovalues 0.2 : 0.2 : 5.2

Density at t= 0.8s, isovalues 2.0 : 1.0 : 13.0

Velocity modulus at t= 0.8s, isovalues 0.2 : 0.2 : 5.6

Density at t= 1.0s, isovalues 2.0 : 1.0 : 10.0

Velocity modulus at t= 1.0s, isovalues 0.2 : 0.2 : 5.6

Figure 6: Density (left column) and speed magnitude (right column) at physical times t=0.2 s, 0.4 s, 0.6 s, 0.8 s and 1.0 s (from top to bottom).

The system (12) is solved on the dimensionless domain $\Omega = [0,9]\times[0,2.67]$, during the dimensionless time interval $0 \leq t \leq 25$ with $\mu(\rho) = \rho$. Results are displayed in Figure 7. The correspondence between Figures 6 and 7 shows that the definition of the dimensionless parameters Fr and Re is clearly relevant. If U is defined as the averaged front speed deduced from Figure 6 (namely $\mathrm{U} = 2.2\, m\, s^{-1}$), then we obtain $\mathrm{Re} = 660, \mathrm{Fr} = 1.28, \mathrm{Sc} = 1.0$, and the results are again very similar to those in Figure 7. We can deduce that the dimensionless process in this range of parameters is not very sensitive to the chosen velocity scale U.

2.4 Parametric Study on the Schmidt, the Froude and the Reynolds Numbers in Avalanches

As said above, the physical features of the avalanches are embodied into the dimensionless parameters Fr, Re, Sc. For real avalanches, the Reynolds number Re can be as large as 10^8 (with front speed of the order of 100 ms^{-1}) and the densimetric Froude number Fr_d is close to 1. However, for experimental devices in laboratory, the values of the parameters are less extreme and become affordable for numerical experiments. We propose here a parametric study on the Froude, Reynolds and Schmidt numbers, inspired by an experimental device developped in [54, 55, 56, 58]. A mixture of salt water and kaolin is released from a small tank along an inclined plane into a larger water tank. Furthermore, the flow is confined to a channel so that lateral spreading is negligible and the features of the flow can be considered as 2-dimensional. The physical domain considered here is the rectangle $[0, 2.0\, m] \times [0, 0.5\, m]$. The slope of the ground is defined by $g/\|g\| = (\sin 10°, -\cos 10°)^T$, with $\|g\| = 9.8\, m\, s^{-2}$. The fluid is initially at rest, and the initial condition on the density is given by:

$$\rho_0(x,y) = \begin{cases} \bar{\rho}_f & \text{for } 0 \leq x \leq 0.15\, m \text{ and } 0 \leq y \leq 0.09\, m, \\ \bar{\rho}_d & \text{otherwise,} \end{cases}$$

with $\bar{\rho}_f = 1.2\, 10^3\, kg\, m^{-3}$ and $\bar{\rho}_d = 10^3\, kg\, m^{-3}$. It yields $\Delta\rho/\bar{\rho}_d = 0.2$. As reported in Figure 8 (extracted from [55]), the measured velocity of the front at the beginning of the simulation is equal to $\mathrm{U} = 0.35\, m\, s^{-1}$; it serves as the reference velocity unit. The length of reference is defined by the initial height of the avalanche ($L = 0.09\, m$), so that the computational domain corresponds to the rectangle $[0, 22] \times [0, 5.5]$, and the reference kinematic viscosity is set to $\bar{\nu} = 1.575 \times 10^{-5}\, m^2\, s^{-1}$. Consequently, the corresponding Froude and Reynolds coefficients defined in (13) are given by:

$$\mathrm{Fr} = 0.3725, \quad \mathrm{Re} = 1000.$$

Let us note that these parameters correspond to a densimetric Froude number $\mathrm{Fr}_d = 0.83$. We also consider the Schmidt number $\mathrm{Sc} = 1$, which is similar to the usual values reported in the bibliography (see [28], [24] and the references therein). This is equivalent to take $\kappa = 3.15 \times 10^{-5}\, m^2\, s^{-1}$. Note that for these simulations, a constant viscosity $\mu(\rho) \equiv 1$ is assumed in (12). The boundary conditions (Dirichlet for the velocity, Neumann for the density) are given by (14). In particular, friction on the ground is neglected.

The computational time step is set to $\Delta t = 10^{-3}$, and an adaptive mesh refinement strategy, based on `BAMG`, is used in order to follow the avalanche front, like in [27, 29, 30]. For the simulations presented here, the smallest convex radius in the mesh oscillates around $h_{\min} \approx 0.0015$ and

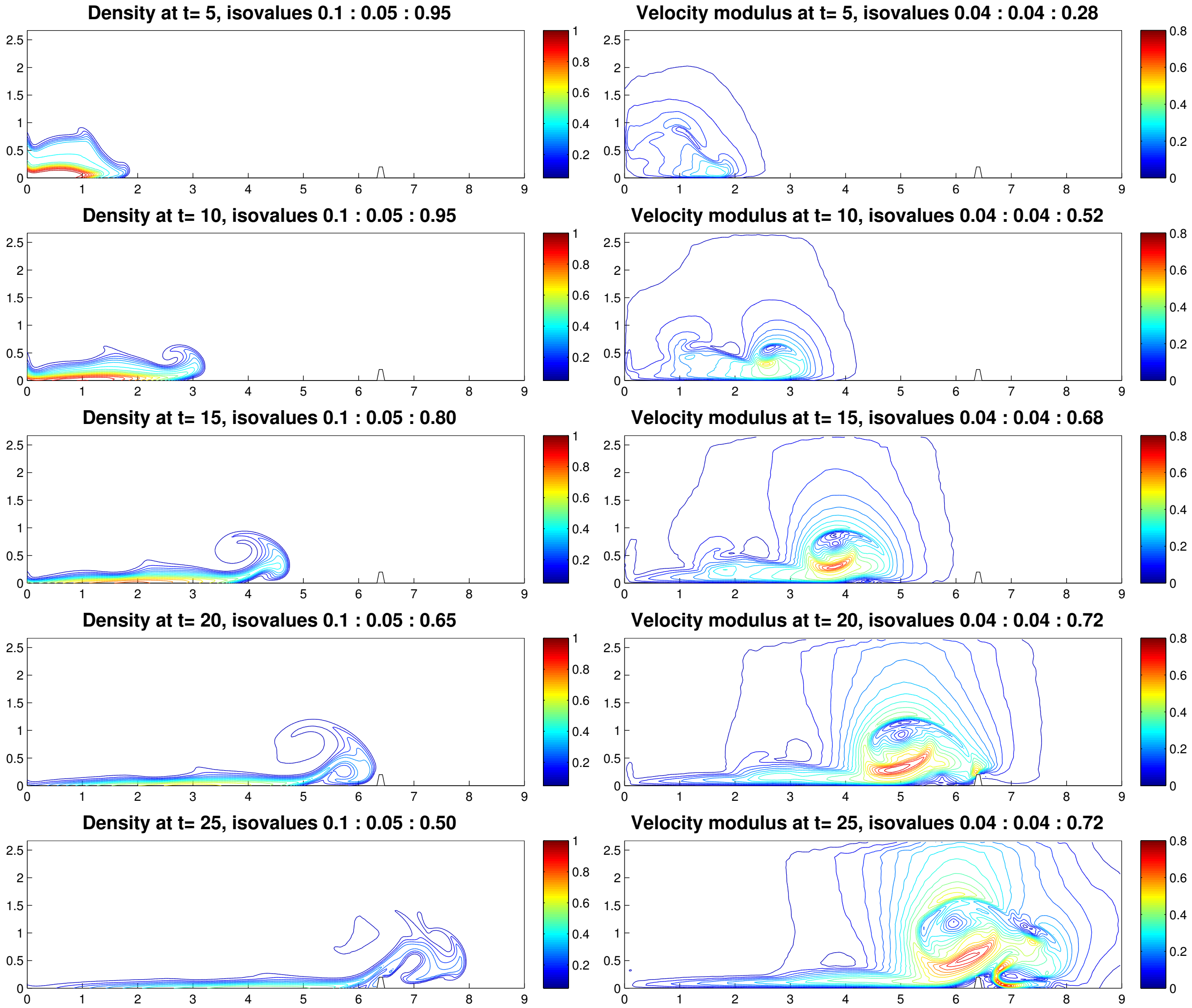

Figure 7: Dimensionless density (left column) and speed magnitude (right column) at dimensionless times $t = 5, 10, 15, 20, 25$ (corresponding to physical times t=0.2 s, 0.4 s, 0.6 s, 0.8 s and 1.0 s (from top to bottom), using (12) with Re = 2242, Fr = 4.3589 and $Sc = 1.0$.

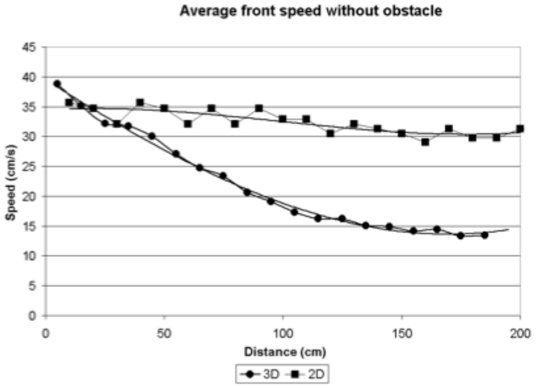

Figure 8: Reference front speed of the avalanche for 2-D and 3-D configurations (Reproduced from [55]).

the maximum length of the edges is of the order $h_{\max} \approx 0.1$. Going back to physical units, it means $h_{\min} \approx 0.00015\,m$ to be compared to $0.005\,m$ for the simulations in [54, 55, 56, 58] made on a fixed grid, refined next to the ground. The number of triangles in the mesh increases up to 50 000 during the simulation. All convergence grid tests have been performed to ensure that the mesh as well as the time step are fine enough to reach the grid convergence.

The evolution of the density and of the speed magnitude during the avalanche are displayed in Figure 9, with a zoom in Figure 10. Qualitatively, the mesh refinement strategy used in the simulation allows us to capture details of the complex structures of the Kelvin-Helmholtz and Rayleigh-Taylor instabilities occurring in the vicinity of the front. It has been constantly observed that the maximal speed is recorded behind the front, and it can reach a value noticeably larger than the front speed [24, 27, 30, 45, 54, 55]. This effect is also clearly visible in our simulations. We also note on the velocity snapshots that a large domain is affected by the avalanche motion, a significant part of the surrounding light fluid is dragged by the snow release; the model reproduces the entrainment of the ambient air.

In order to allow some comparisons with the experimental data given in [58], we come back to the dimensional values. The horizontal velocity has been recorded at two monitoring points A and B with coordinates $(50\,cm, 2.7\,cm)$ and $(50\,cm, 6.7\,cm)$, respectively. Note that the origin is not placed at the same location in [55] and needs to be horizontally shifted by $62\,cm$ to compare the corresponding results with ours. Experimental measurements are reported in Figure 11 (point A on the top, point B at the bottom). These data have to be considered with caution, since there are many sources of uncertainties due to the measurements techniques. On the one hand, the velocity is evaluated by Doppler ultrasonic velocimetry techniques, which are sensible to the particles concentration. We refer the reader to the discussion in [55, sp. Section 4.1] about the corresponding sources of uncertainties, and how they can be taken into account in the interpretation of the results. On the other hand, the release is not well-determined, and Figure 11 represents data averaged over several experimental runs, after having decided that the maximal velocity is reached

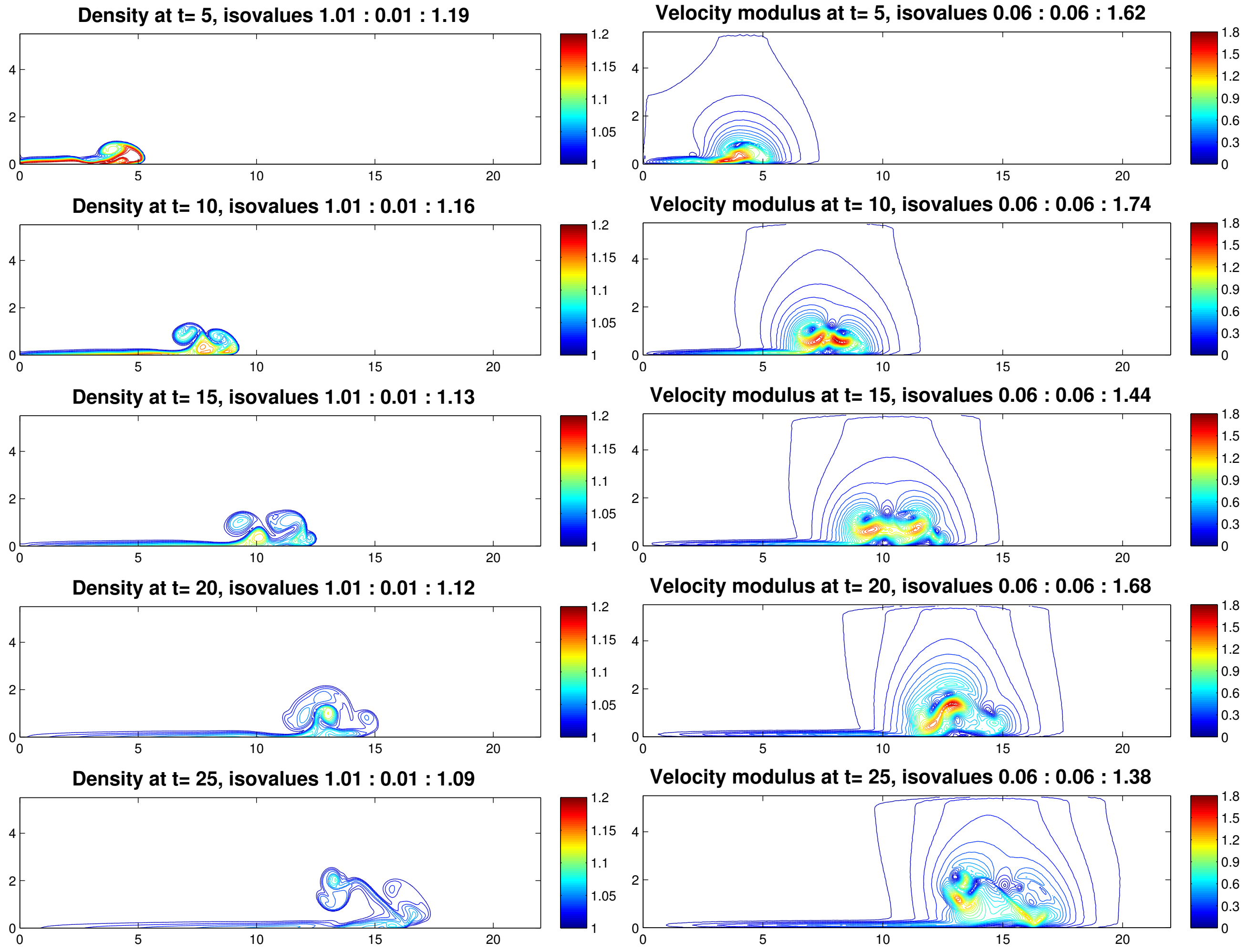

Density at t= 5, isovalues 1.01 : 0.01 : 1.19

Velocity modulus at t= 5, isovalues 0.06 : 0.06 : 1.62

Density at t= 10, isovalues 1.01 : 0.01 : 1.16

Velocity modulus at t= 10, isovalues 0.06 : 0.06 : 1.74

Density at t= 15, isovalues 1.01 : 0.01 : 1.13

Velocity modulus at t= 15, isovalues 0.06 : 0.06 : 1.44

Density at t= 20, isovalues 1.01 : 0.01 : 1.12

Velocity modulus at t= 20, isovalues 0.06 : 0.06 : 1.68

Density at t= 25, isovalues 1.01 : 0.01 : 1.09

Velocity modulus at t= 25, isovalues 0.06 : 0.06 : 1.38

Figure 9: Density (left column) and speed magnitude (right column) at dimensionless times t from 5 to 25 (from top to bottom) with $Sc = 1.0$, $\mathrm{Fr} = 0.3725$ and $\mathrm{Re} = 1000$.

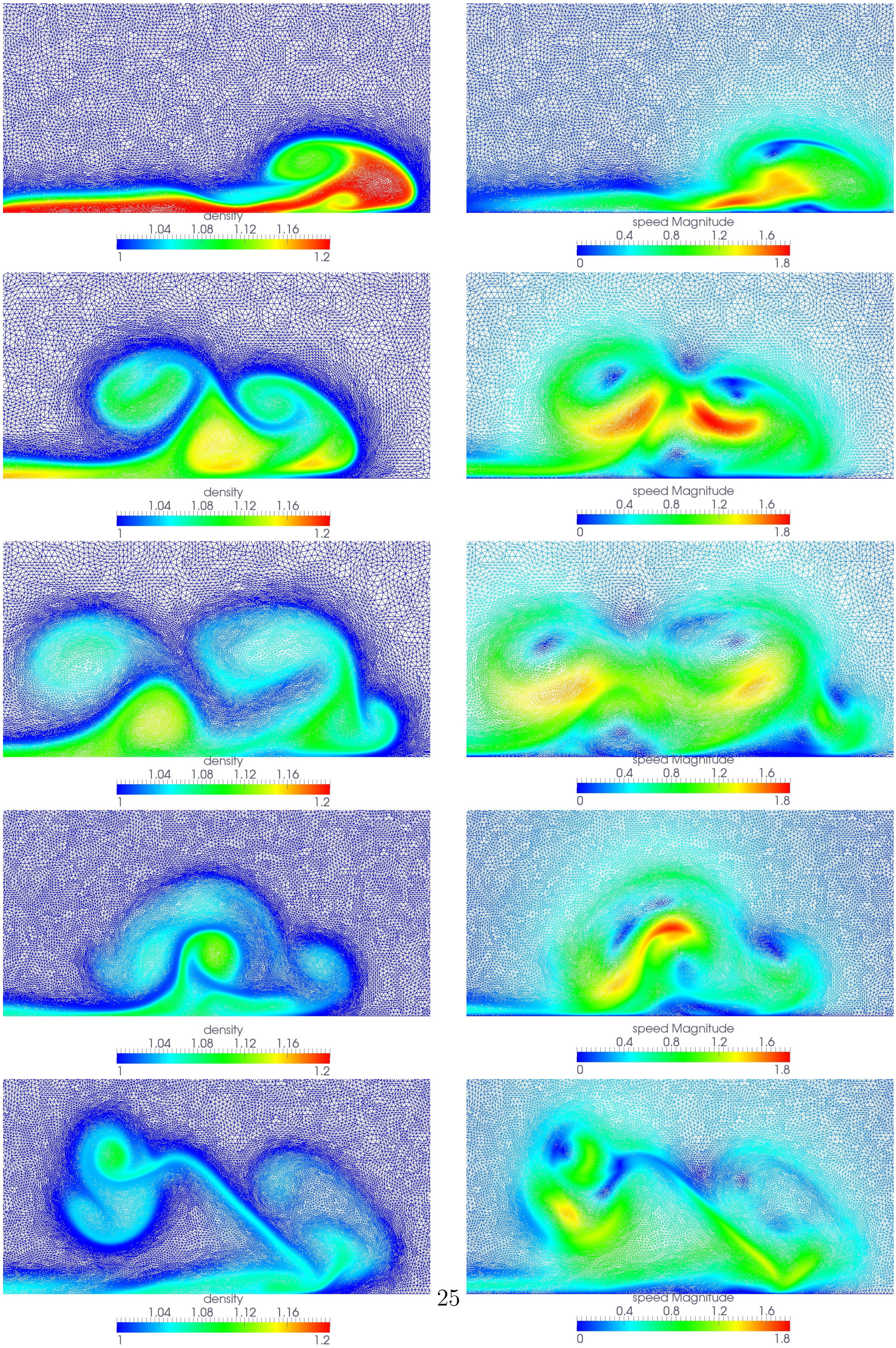

Figure 10: Density (left column) and speed magnitude (right column) at dimensionless times t from 5 to 25 (from top to bottom) with $\mathrm{Sc} = 1.0$, $\mathrm{Fr} = 0.3725$ and $\mathrm{Re} = 1000$, zoom of Figure 9.

at the same time. We compare the experimental horizontal velocity at node A (resp. B) in Figure 11 to the numerical results computed at the same nodes (plain blue, resp. dotted black, line in Figure 12). For both nodes, it can be observed that the maximal value of the numerical horizontal velocity is in good agreement with the laboratory experiments (namely $0.45\, m\, s^{-1}$ at node A and nearly $0.40\, m\, s^{-1}$ at node B). However, we observe two peaks in Figure 12 compared to a single peak in Figure 11. We do not know whether or not this phenomenon is physical and whether or not the measurements techniques could detect it. The behavior might be also due to the no-slip condition imposed to the velocity. In Figure 10, the zoom shows very clearly the development of a Rayleigh-Taylor instability near the horizontal boundary. Small scale perturbations grow with time, developing a vortex which lives and rolls up near the boundary. These perturbations induce the separation of the dense phase into two quite-detached parts, exactly when the front of the avalanche passes in front of the monitoring points A and B. Considering other boundary conditions, as for example a friction law, can solve this discrepancy with the experiment. We should mention here that the simulation might be sensitive to mesh orientation effects and the treatment of the boundary conditions, see [16]. These aspects should be discussed in further details, with an interaction with experimentalists.

Finally, using the values of the parameters defined by the laboratory experiments as a reference, we investigate numerically how their variation influence the flow.

2.4.1 Influence of the Schmidt Number

The Schmidt number is the less clear of the three parameters that govern the flow, it highly relies on the modeling assumptions and it is not easily accessible to measurements. The choice $\mathrm{Sc} = 1$ is made in [27, 30], and $\mathrm{Sc} = 0.7$ is set in [54, 55, 56, 58]. When the Schmidt number goes to infinity, the model (12) degenerates into the incompressible inhomogeneous Navier-Stokes system. We consider here the reference simulation ($\mathrm{Sc} = 1.0$, $\mathrm{Fr} = 0.3725$, $\mathrm{Re} = 1000$, see Figure 9), and we make the Schmidt number vary, namely $\mathrm{Sc} = \infty$ (Figure 13), $\mathrm{Sc} = 10$ (Figure 14) and $\mathrm{Sc} = 0.1$ (Figure 15). The solution of (12) for $\mathrm{Sc} = 1.0$ (more or less the value given in the literature) given in Figure 9 significantly differs from the solution of the incompressible case given in Figure 13. This observation justifies that the mere incompressible system misses effects relevant for mixture flows. As expected, for finite Sc, the density exhibits a more diffusive behavior, which impacts on the maximum velocity recorded in the domain. Figure 14 shows that with $\mathrm{Sc} = 10$, the diffusion remains weak compared to $\mathrm{Sc} = \infty$, whereas in Figure 15 corresponding to $Sc = 0.1$ the density diffusion is very high, and the whole simulation strongly changes. Indeed, the smaller Sc, the more important the diffusive behavior induced by the Fick law. Nevertheless, the velocity of the front of the avalanche does not vary significantly.

2.4.2 Influence of the Reynolds Number

Next, we investigate the influence of the Reynolds number. We start from the reference simulation ($\mathrm{Sc} = 1.0$, $\mathrm{Fr} = 0.3725$, $\mathrm{Re} = 1000$, Figure 9), and we make the Reynolds number vary, namely $\mathrm{Re} = 3000$ (Figure 16) and $\mathrm{Re} = 5000$ (Figure 17). As the Reynolds number increases, the number of triangles in the mesh increases too (here up to 100 000). This is necessary in order to preserve

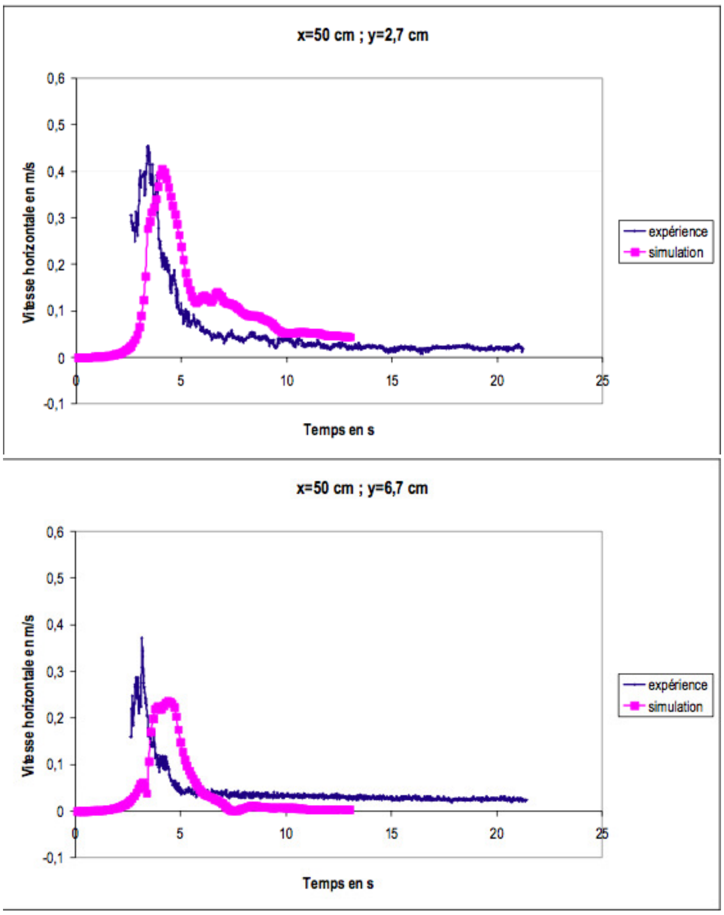

Figure 11: Records and simulations (with a k/ϵ model) of the horizontal velocity at the monitoring points A (top), B (bottom). Reproduced from [58].

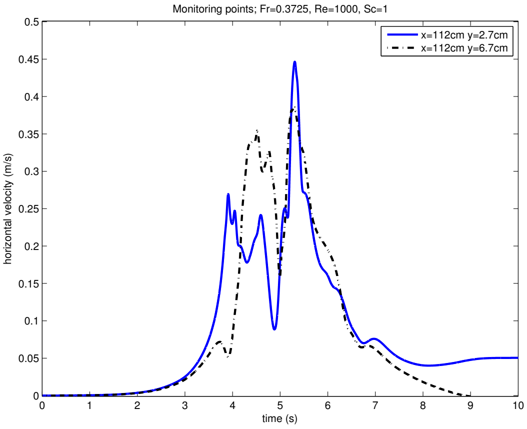

Figure 12: Horizontal velocity computed at the monitoring points A and B. $Fr = 0.3725$, $Re = 1000$, $Sc = 1$.

the grid convergence property. Indeed, high Reynolds numbers require finer meshes to resolve the fine scales, a typical feature of Direct Numerical Simulation. In agreement to observations made with the classical Navier-Stokes system, when the Reynolds number becomes large the maximal modulus of velocity recorded in the domain (and, here, the front speed of the avalanche) slightly increases. The more significant differences as Re varies are observed in the detailed structures of the solutions, characterized for large Re's by the formation of many vortices typical of a turbulent behavior.

2.4.3 Influence of the Froude Number

Finally, we study the influence of the Froude number. From the reference simulation (Sc = 1.0, Fr = 0.3725, Re = 1000, Figure 9), we modify the Froude number, namely Fr = 0.6 (Figure 18) and Fr = 1.0 (Figure 19). When the Froude number increases, the strength of the external force decreases and a deceleration of the front of the avalanche is observed, according to the physical intuition. This can be seen in the evolution of the speed magnitude. Considering the same position of the front of the avalanche, the structures of the flow remain quite similar for the three different Froude numbers, although the corresponding physical times are not the same, of course. Besides, it is worth pointing out that variations of the Froude number strongly impact the computational cost: the smaller Fr, the more demanding the simulation. Indeed, as Fr decreases, finer meshes are necessary to reach the grid convergence. Thus, the reference avalanche, with Fr = 0.3725, is definitely more challenging than the test case addressed in Sections 2.3.1– 2.3.2.

3 Conclusion

In this work we discuss a hierarchy of models, including connection to the Eulerian-Lagrangian description, for mixtures flows, which applies to many environmental flows. These models are

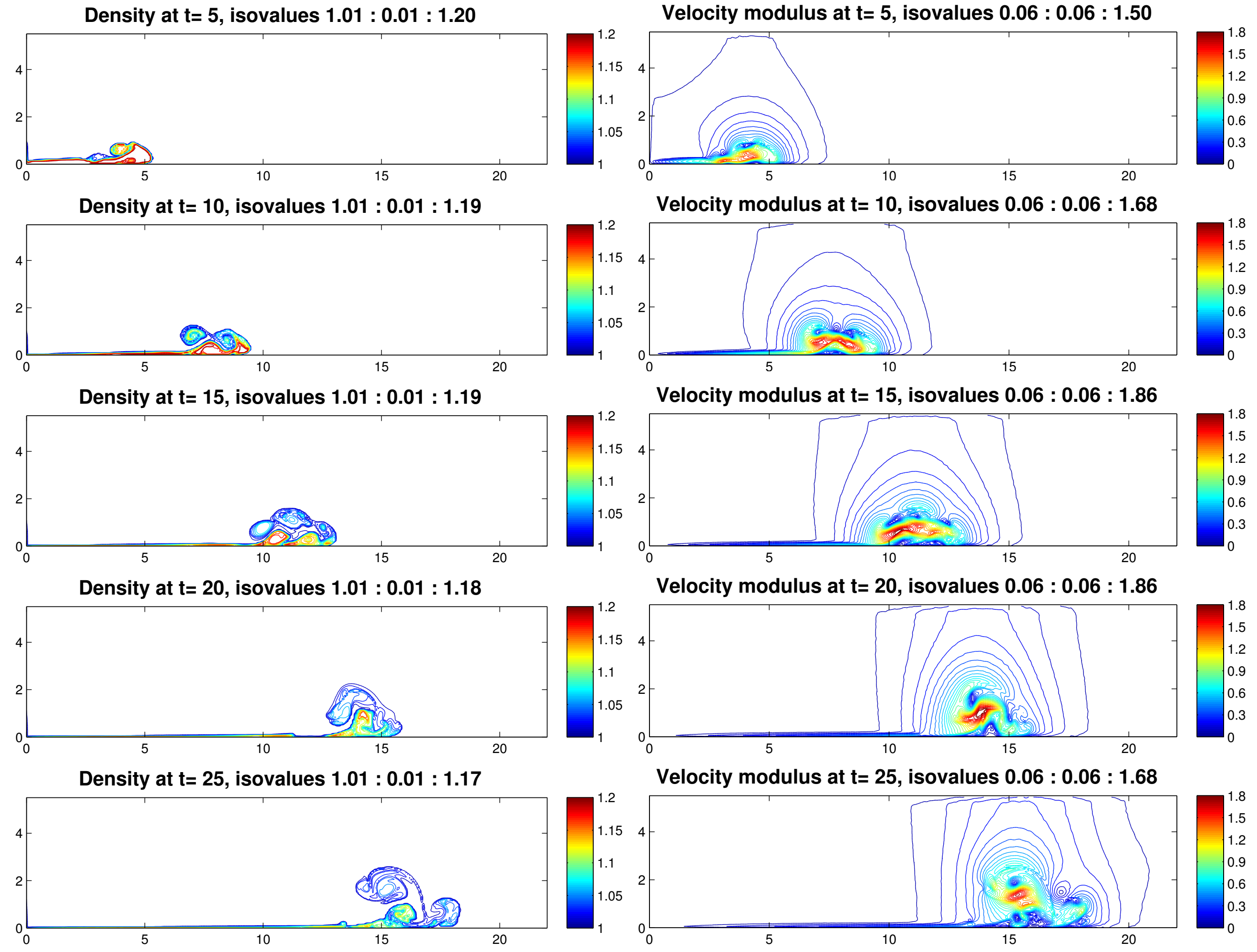

Figure 13: Density (left column) and speed magnitude (right column) at dimensionless times t from 5 to 25 (from top to bottom) with $\mathrm{Sc} = \infty$, $\mathrm{Fr} = 0.3725$ and $\mathrm{Re} = 1000$.

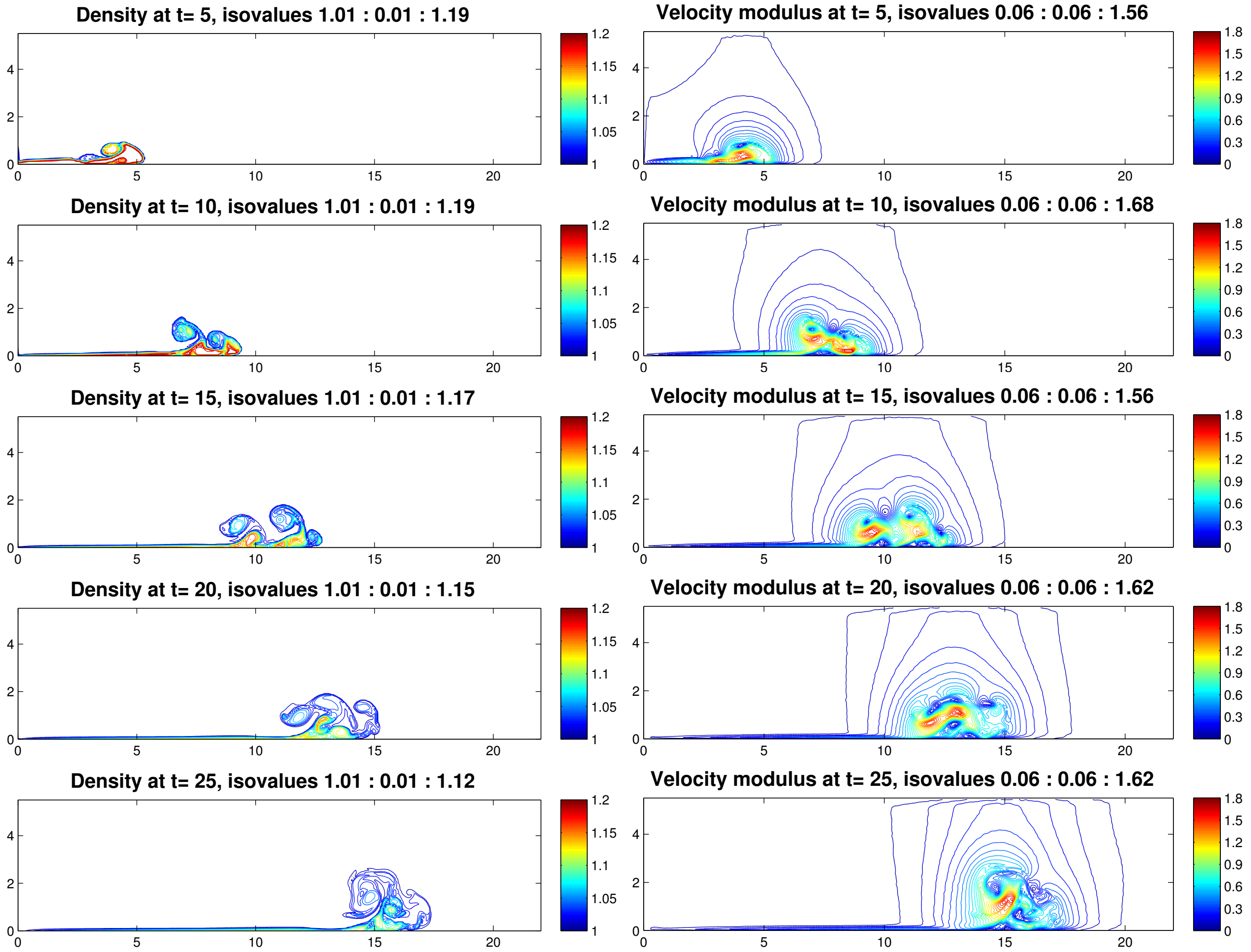
Density at t= 5, isovalues 1.01 : 0.01 : 1.19

Velocity modulus at t= 5, isovalues 0.06 : 0.06 : 1.56

Density at t= 10, isovalues 1.01 : 0.01 : 1.19

Velocity modulus at t= 10, isovalues 0.06 : 0.06 : 1.68

Density at t= 15, isovalues 1.01 : 0.01 : 1.17

Velocity modulus at t= 15, isovalues 0.06 : 0.06 : 1.56

Density at t= 20, isovalues 1.01 : 0.01 : 1.15

Velocity modulus at t= 20, isovalues 0.06 : 0.06 : 1.62

Density at t= 25, isovalues 1.01 : 0.01 : 1.12

Velocity modulus at t= 25, isovalues 0.06 : 0.06 : 1.62

Figure 14: Density (left column) and speed magnitude (right column) at dimensionless times t from 5 to 25 (from top to bottom) with $\mathrm{Sc} = 10$, $\mathrm{Fr} = 0.3725$ and $\mathrm{Re} = 1000$.

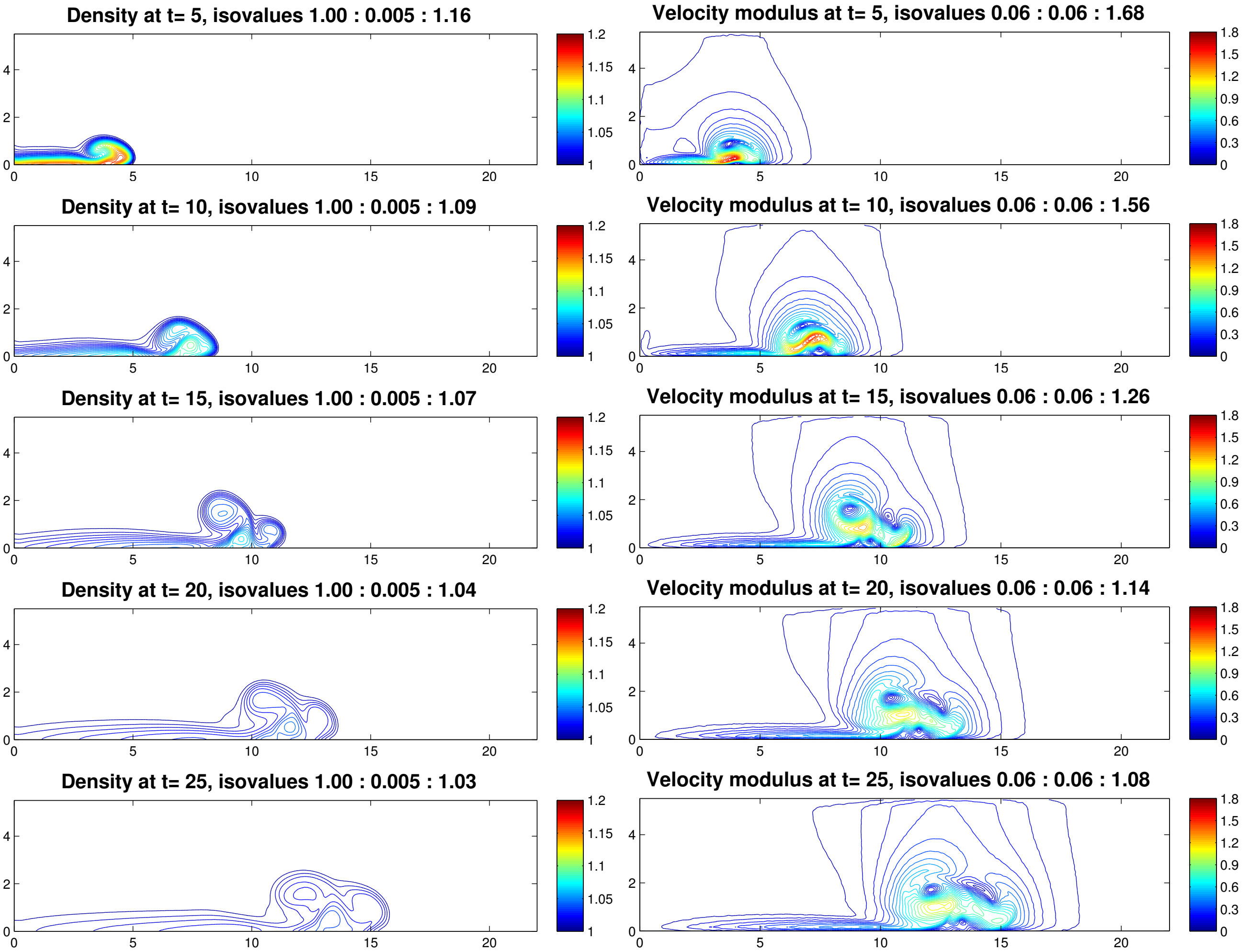

Figure 15: Density (left column) and speed magnitude (right column) at dimensionless times t from 5 to 25 (from top to bottom) with $\mathrm{Sc} = 0.1$, $\mathrm{Fr} = 0.3725$ and $\mathrm{Re} = 1000$.

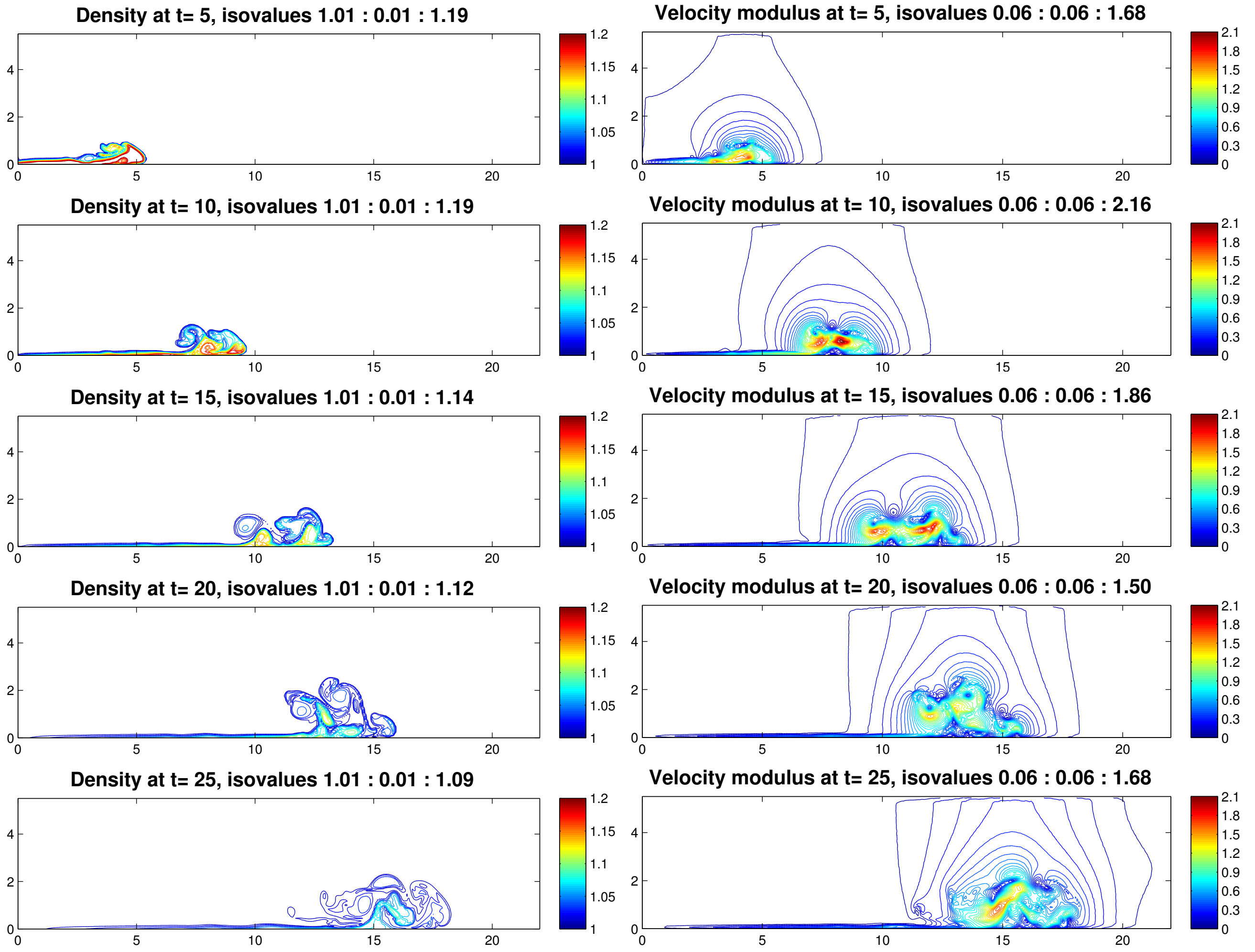
Density at t= 5, isovalues 1.01 : 0.01 : 1.19

Velocity modulus at t= 5, isovalues 0.06 : 0.06 : 1.68

Density at t= 10, isovalues 1.01 : 0.01 : 1.19

Velocity modulus at t= 10, isovalues 0.06 : 0.06 : 2.16

Density at t= 15, isovalues 1.01 : 0.01 : 1.14

Velocity modulus at t= 15, isovalues 0.06 : 0.06 : 1.86

Density at t= 20, isovalues 1.01 : 0.01 : 1.12

Velocity modulus at t= 20, isovalues 0.06 : 0.06 : 1.50

Density at t= 25, isovalues 1.01 : 0.01 : 1.09

Velocity modulus at t= 25, isovalues 0.06 : 0.06 : 1.68

Figure 16: Density (left column) and speed magnitude (right column) at dimensionless times t from 5 to 25 (from top to bottom) with $\mathrm{Sc} = 1$, $\mathrm{Fr} = 0.3725$ and $\mathrm{Re} = 3000$.

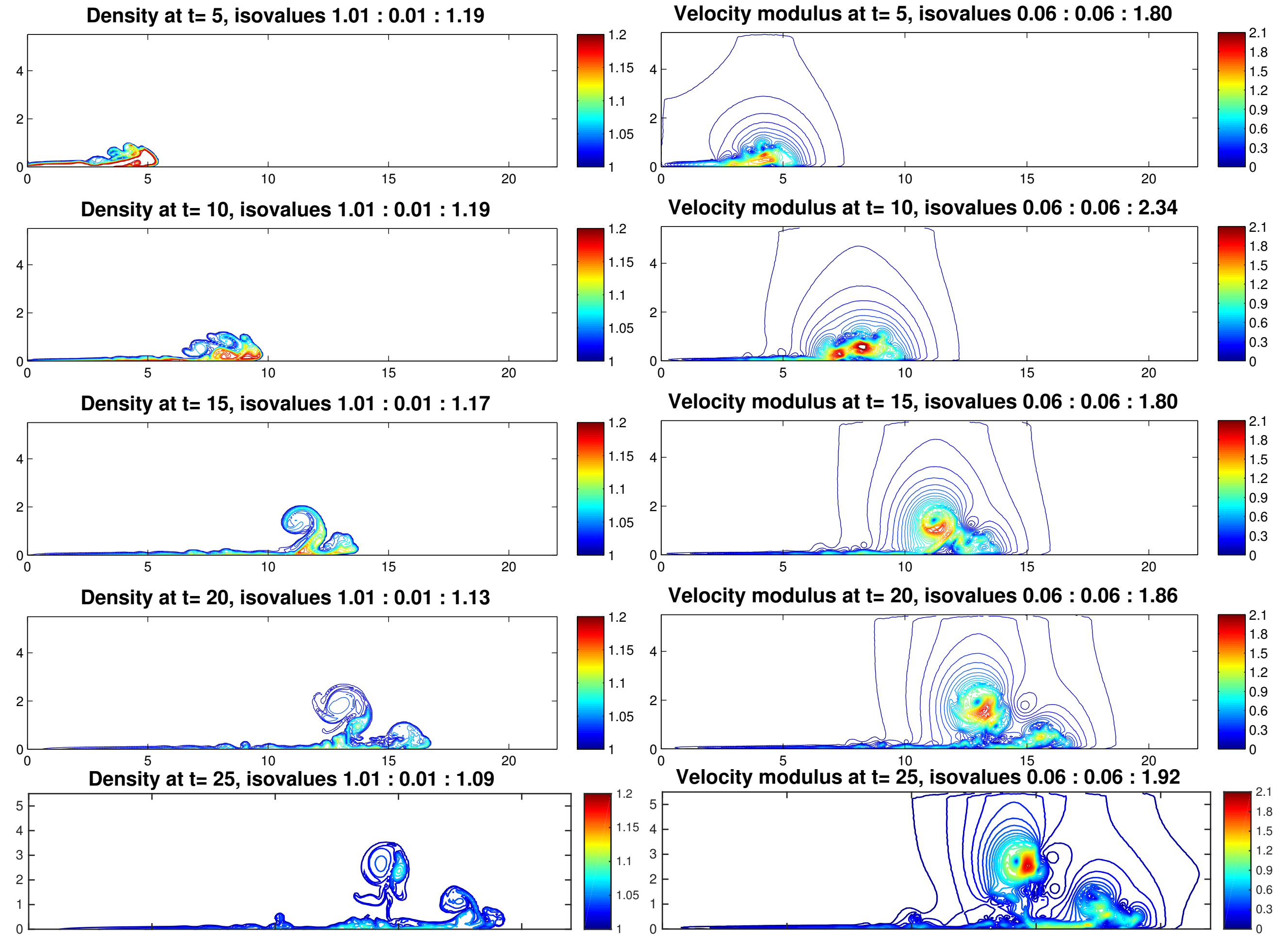
Density at t= 5, isovalues 1.01 : 0.01 : 1.19

Velocity modulus at t= 5, isovalues 0.06 : 0.06 : 1.80

Density at t= 10, isovalues 1.01 : 0.01 : 1.19

Velocity modulus at t= 10, isovalues 0.06 : 0.06 : 2.34

Density at t= 15, isovalues 1.01 : 0.01 : 1.17

Velocity modulus at t= 15, isovalues 0.06 : 0.06 : 1.80

Density at t= 20, isovalues 1.01 : 0.01 : 1.13

Velocity modulus at t= 20, isovalues 0.06 : 0.06 : 1.86

Density at t= 25, isovalues 1.01 : 0.01 : 1.09

Velocity modulus at t= 25, isovalues 0.06 : 0.06 : 1.92

Figure 17: Density (left column) and speed magnitude (right column) at dimensionless times t from 5 to 25 (from top to bottom) with $\mathrm{Sc} = 1$, $\mathrm{Fr} = 0.3725$ and $\mathrm{Re} = 5000$.

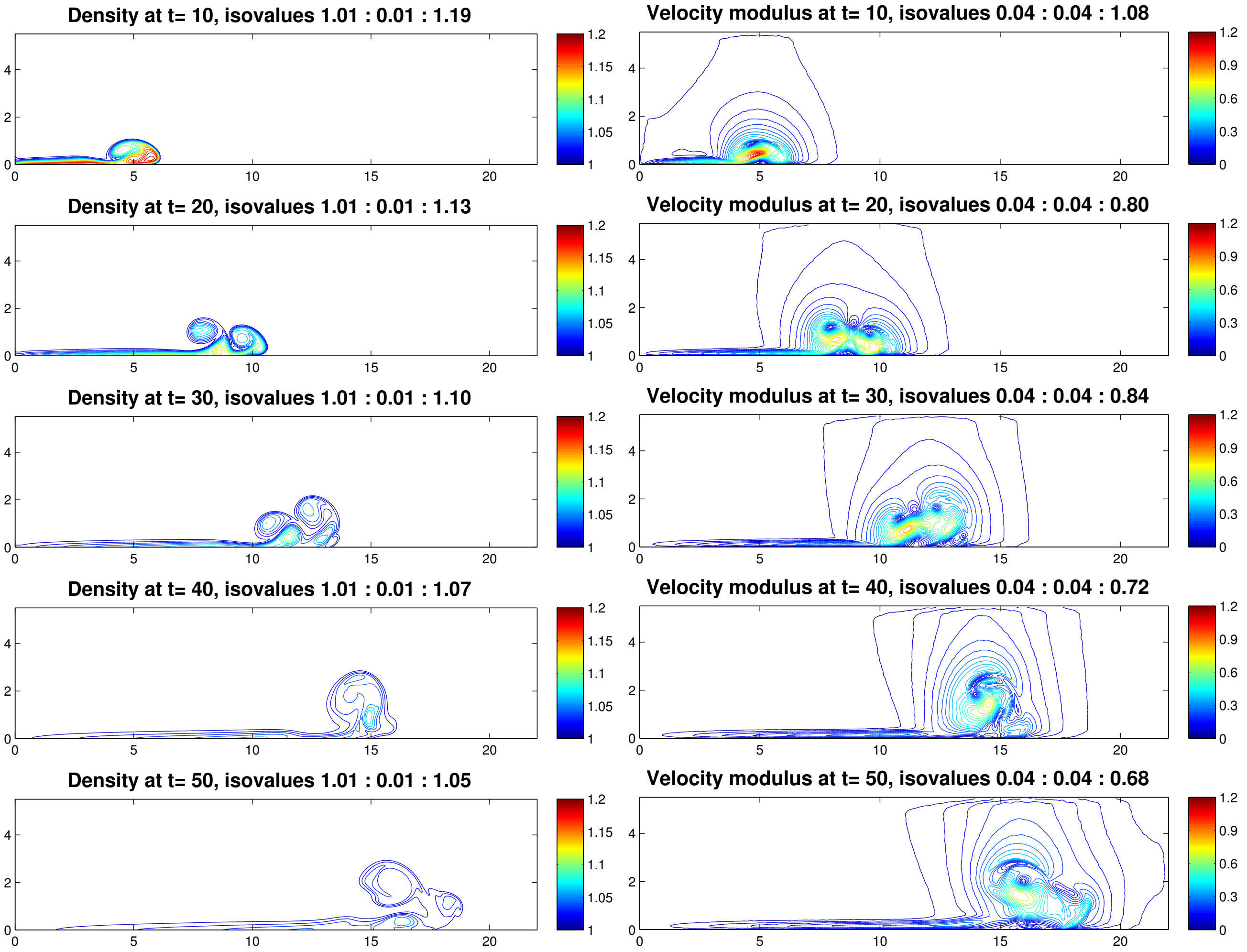

Density at t= 10, isovalues 1.01 : 0.01 : 1.19

Velocity modulus at t= 10, isovalues 0.04 : 0.04 : 1.08

Density at t= 20, isovalues 1.01 : 0.01 : 1.13

Velocity modulus at t= 20, isovalues 0.04 : 0.04 : 0.80

Density at t= 30, isovalues 1.01 : 0.01 : 1.10

Velocity modulus at t= 30, isovalues 0.04 : 0.04 : 0.84

Density at t= 40, isovalues 1.01 : 0.01 : 1.07

Velocity modulus at t= 40, isovalues 0.04 : 0.04 : 0.72

Density at t= 50, isovalues 1.01 : 0.01 : 1.05

Velocity modulus at t= 50, isovalues 0.04 : 0.04 : 0.68

Figure 18: Density (left column) and speed magnitude (right column) at dimensionless times t from 10 to 50 (from top to bottom) with $\mathrm{Sc} = 1.0$, $\mathrm{Fr} = 0.6$ and $\mathrm{Re} = 1000$.

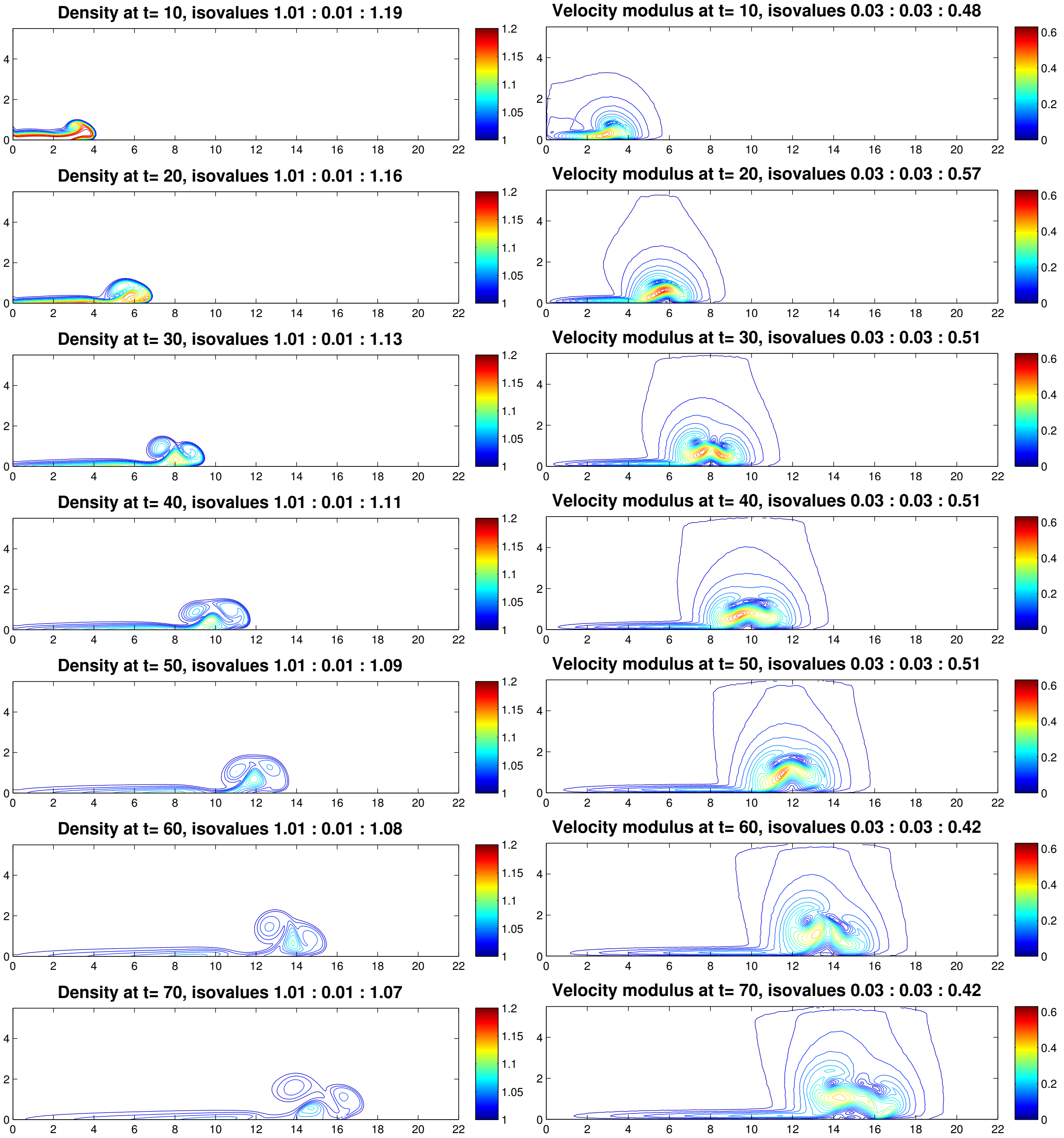

Figure 19: Density (left column) and speed magnitude (right column) at dimensionless times t from 10 to 70 (from top to bottom) with $\mathrm{Sc} = 1.0$, $\mathrm{Fr} = 1.0$ and $\mathrm{Re} = 1000$.

characterized by diffusive fluxes between the different components of the mixture, which induce new constraints in the PDEs system. We propose a specific numerical scheme to simulate the behavior of such systems. The method is based on a time-splitting approach and a hybrid Finite Volume-Finite Element scheme which have shown their efficiency for non homogeneous incompressible flows. This numerical approach is reliable : the possibility of working on unstructured meshes, and thus of coupling the resolution with mesh refinement strategies, make it well-adapted to follow complex fronts typical of mixture flows. The scheme is validated through comparison to analytical solutions: the new coupling terms are treated without degrading the accuracy of the scheme. Furthermore, we check that the method supports mesh perturbations. The method is used to investigate avalanche phenomena. A comparison with numerical simulations, based on different techniques, and experimental data available in the literature is discussed. Finally, we study on numerical grounds the role of the physical parameters of the flows. It demonstrates the skills and the robustness of the method.

Aknowledgements

We are indebted to Didier Bresch and Céline Acary-Robert for very fruitful discussions about this work and for friendly advices on the simulations of avalanches, as well as the referees who allow us to significantly improve the paper. This work is partially supported by the Labex CEMPI (ANR-11-LABX-0007-01).

A A derivation from the Eulerian–Lagrangian modeling

We propose in this Appendix a possible derivation of the constraint (3) starting form a Eulerian–Lagrangian description of the mixture.

A.1 Introduction to the model

In this Section the disperse phase is thought of as a large set of droplets (for instance it can be applied to aerosols powder-snow avalanches). This description involves a coupling between the mass and momentum conservation for the fields (ρ_f, u_f) characterizing the fluid and a kinetic equation satisfied by the particle distribution function $F(t, x, \xi)$ describing the dilute phase. In other words, the dilute phase is seen as a set of disperse particles for which we adopt a statistical viewpoint: $F(t, x, \xi)\,\mathrm{d}\xi\,\mathrm{d}x$ corresponds to the number of particles of the disperse phase having at time t their position and velocity in the infinitesimal domain centered at (x, ξ) with volume $\mathrm{d}\xi\,\mathrm{d}x$. This modeling applies for particles suspension where a typical measure of the size of the particles is small compared to the interparticles distance. From now on, we discuss the modeling issues considering the natural three-dimensional framework. Assuming that particles are spherically shaped with radius $a > 0$,

$$\phi(t, x) = \frac{4}{3}\pi a^3 \int_{\mathbb{R}^3} F(t, x, \xi)\,\mathrm{d}\xi$$

is interpreted as the volume fraction occupied by the particles. We define accordingly the mass density and momentum of the disperse phase

$$\rho_d(t, x) = \bar{\rho}_d \phi(t, x), \qquad \rho_d u_d(t, x) = \bar{\rho}_d \phi u_d(t, x) = \frac{4}{3}\pi a^3 \bar{\rho}_d \int_{\mathbb{R}^3} \xi F(t, x, \xi)\,\mathrm{d}\xi.$$

The system of PDEs describing the behavior of the mixture reads as follows. We write the mass and momentum conservation equation for the dense phase, namely

$$\begin{aligned} \partial_t \rho_f + \nabla_x \cdot (\rho_f u_f) &= 0, \\ \partial_t(\rho_f u_f) + \mathrm{Div}_x(\rho_f u_f \otimes u_f) + \nabla_x p &= \rho_f g + \mathrm{Div}_x\big(2\mu \mathbb{D}(u_f)\big) + \mathrm{Drag}_f \end{aligned} \tag{20}$$

where the last term in the momentum equation accounts for the drag force exerted by the particles on the fluid. The particle distribution function $F(t, x, \xi)$ obeys

$$\partial_t F + \xi \cdot \nabla_x F + g \cdot \nabla_\xi F = \nabla_\xi \cdot \Big(- \mathrm{Drag}_d\ F + D \nabla_\xi F \Big). \tag{21}$$

In this equation we take into account gravity effects on the particles that give rise to the acceleration term $g \cdot \nabla_\xi F$, with g the gravitational acceleration. The right hand side in (21) describes both the drag force exerted by the fluid on the particles and the Brownian motion of the particles. Brownian motion induces diffusion with respect to the velocity variable, with a diffusion coefficient defined by the following Einstein formula [25]

$$D = \frac{9\mu}{2\bar{\rho}_d a^2} \frac{3k\theta}{4\pi a^3 \bar{\rho}_d},$$

where μ is the dynamic viscosity of the fluid, θ is the temperature of the flow, assumed a fixed positive constant and k stands for the Boltzmann constant. The expression of the drag force can be a quite intricate and non linear function, derived from phenomelogical considerations and depending on the densities ρ_f, ρ_d, the viscosity μ, the radius a and the relative velocity $\xi - u$. Here we restrict ourselves to the situation where it is given by the Stokes law, hence a linear function of the relative velocity

$$-\mathrm{Drag}_d = \frac{9\mu}{2a^2\bar{\rho}_d}\ Z(\phi)\ (\xi - u_f)$$

with a certain (dimensionless) function $Z : [0,\infty) \to [0,\infty)$. Note that the viscosity itself might be a function of the volume fraction ϕ. The right hand side in (21) then becomes

$$\frac{9\mu}{2a^2\bar{\rho}_d}\nabla_\xi \cdot \Big(Z(\phi)(\xi - u_f)F + \frac{3k\theta}{4\pi a^3\bar{\rho}_d}\nabla_\xi F\Big).$$

We refer the reader for instance to [25] or more recently [37] for a thorough discussion on this Fokker–Planck operator. The drag force exerted on the fluid by the particles is the back–reaction to the drag force exerted by the fluid on the particles. Hence, taking into account all particles located at position x it is defined by the velocity average

$$\mathrm{Drag}_f = -\frac{4}{3}\pi a^3\bar{\rho}_d \int_{\mathbb{R}^3} \mathrm{Drag}_d\ F\,\mathrm{d}\xi.$$

(Note that with our convention Drag_d is homogeneous to $\frac{\text{Velocity}}{\text{Time}}$, while Drag_f is homogeneous to $\frac{\text{Mass}\times\text{Velocity}}{\text{Volume}\times\text{Time}}$.) As a matter of fact, we can write

$$\mathrm{Drag}_f = 6\pi\mu a\ Z(\phi) \int_{\mathbb{R}^3} (\xi - u_f)F\,\mathrm{d}\xi = \frac{9\mu}{2a^2\bar{\rho}_d}\ Z(\phi)\ \rho_d(u_d - u_f).$$

The model is closed by setting

$$\rho_f(t,x) = \bar{\rho}_f\big(1 - \phi(t,x)\big).$$

In other words, we assume here that the fluid is incompressible in the sense that the mass density remains constant in the domain occupied by the dense phase; nevertheless we account locally for the volume occupied by the particles in the mass and momentum balance. Observe that $\phi(t,x) \geq 0$ but there is no reason guaranteeing that ϕ remains bounded by 1 (except in the case where u_f is divergence–free: then the first equation in (20) can be rewritten equivalently in non–conservative form, which implies the maximum principle for ϕ). It has to be considered as a modeling assumption: the equations make sense as far as ϕ remains far below 1, which means that the particles are highly dilute. Naturally, we can define the mass density of the mixture by

$$\rho(t,x) = \rho_f(t,x) + \rho_d(t,x) = \bar{\rho}_f\big(1 - \phi(t,x)\big) + \bar{\rho}_d\phi(t,x)$$

and the mean mass velocity is

$$\rho u(t,x) = \rho_f u_f(t,x) + \rho_d u_d(t,x) = \bar{\rho}_f\big(1-\phi(t,x)\big)u_f(t,x) + \frac{4}{3}\pi a^3 \bar{\rho}_d \int_{\mathbb{R}^3} \xi F(t,x,\xi)\,\mathrm{d}\xi.$$

Integrating (21) over the velocity variable we obtain

$$\frac{4}{3}\pi a^3 \bar{\rho}_d \left(\partial_t \int_{\mathbb{R}^3} F\,\mathrm{d}\xi + \nabla_x \cdot \int_{\mathbb{R}^3} \xi F\,\mathrm{d}\xi\right) = 0 = \partial_t \rho_d + \nabla_x \cdot (\rho_d u_d)$$

and, similarly, multiplying (21) by ξ and integrating over the velocity variable, we are led to

$$\begin{aligned}
&\frac{4}{3}\pi a^3 \bar{\rho}_d \left(\partial_t \int_{\mathbb{R}^3} \xi F\,\mathrm{d}\xi + \mathrm{Div}_x \int_{\mathbb{R}^3} \xi\otimes\xi F\,\mathrm{d}\xi - g\int_{\mathbb{R}^3} F\,\mathrm{d}\xi\right)\\
&\qquad = -6\pi\mu a\ Z(\phi) \int_{\mathbb{R}^3} (\xi - u_f)F\,\mathrm{d}\xi = -\frac{9\mu}{2a^2\bar{\rho}_d}\ Z(\phi)\ \rho_d(u_d - u_f)\\
&\qquad = \partial_t(\rho_d u_d) + \mathrm{Div}_x\left(\frac{4}{3}\pi a^3 \bar{\rho}_d \int_{\mathbb{R}^3} \xi\otimes\xi F\,\mathrm{d}\xi\right) - g\rho_d.
\end{aligned}$$

As a matter of fact, combining these relations with (20), we deduce that

$$\begin{aligned}
&\partial_t \rho + \nabla_x \cdot (\rho u) = 0,\\
&\partial_t(\rho u) + \mathrm{Div}_x\Big(\rho_f u_f\otimes u_f + \frac{4}{3}\pi a^3 \bar{\rho}_d \int_{\mathbb{R}^3} \xi\otimes\xi F\,\mathrm{d}\xi\Big) + \nabla_x p = \rho g + \mathrm{Div}_x\big(2\mu\mathbb{D}(u_f)\big)
\end{aligned}$$

holds, that can be interpreted as the total mass conservation and the balance law for the total momentum, respectively. Furthermore, we have

$$\partial_t\Big(\frac{\rho_f}{\bar{\rho}_f} + \frac{\rho_d}{\bar{\rho}_d}\Big) = \partial_t(1-\phi+\phi) = 0 = -\nabla_x \cdot \Big(\frac{\rho_f}{\bar{\rho}_f}u_f + \frac{\rho_d}{\bar{\rho}_d}u_d\Big) = -\nabla_x \cdot \big((1-\phi)u_f + \phi u_d\big).$$

It recasts as a constraint on the velocity field

$$\nabla_x \cdot \big((1-\phi)u_f\big) = -\frac{4}{3}\pi a^3 \nabla_x \cdot \int_{\mathbb{R}^3} \xi F\,\mathrm{d}\xi = -\nabla_x \cdot (\phi u_d).$$

It can be rephrased by saying that the mean volume velocity of the flow is divergence free. We refer for further details on these Eulerian–Lagrangian models to [3, 60, 59, 66]; they are widely used to describe natural or industrial flows like sedimenting and fluidized suspensions, hydraulic fracturing of reservoirs, the dispersion of atmospheric pollutants and dusts...

B Dimensionless equations and hydrodynamic regimes

We wish to derive a hydrodynamic model with the constraint (3) through asymptotic arguments. To this end, we need to make dimensionless parameters appear:

- We introduce time and length scales of reference, say T and L, and we set $\mathrm{U} = \mathrm{L}/\mathrm{T}$ as the velocity unit.
- We define the thermal velocity as to be $\mathrm{V}_{th} = \sqrt{\frac{3k\theta}{4\pi a^3 \bar\rho_d}}$.
- We introduce a typical value $0 < \bar\phi < 1$ of the particle volume fraction (in practice the quantity is quite small compared to 1), and a typical value of the viscosity $\bar\mu$.
- The driving parameters defined by means of the physical properties of the constituents are the Stokes settling time $\frac{2\bar\rho_d a^2}{9\bar\mu}$, and the ratio of the mass densities $\frac{\bar\rho_d}{\bar\rho_f}$. We set
$$\epsilon = \frac{2\bar\rho_d a^2}{9\bar\mu \mathrm{T}}, \qquad \eta = \frac{\mathrm{V}_{th}}{\mathrm{U}}, \qquad \bar g = g\frac{\mathrm{T}^2}{\mathrm{L}}$$
- We define dimensionless variables and unknowns as follows
$$\begin{aligned}
&t = \mathrm{T}t_\star, \qquad x = \mathrm{L}x_\star, \qquad v = \mathrm{V}_{th}v_\star,\\
&F(t,x,v) = \frac{3}{4\pi a^3}\frac{1}{\mathrm{V}_{th}^3}\ \bar\phi\ F_\star(t_\star,x_\star,v_\star),\\
&\phi(t,x) = \bar\phi\ \phi_\star(t_\star,x_\star) = \bar\phi\int_{\mathbb{R}^3} F(t_\star,x_\star,v_\star)\,\mathrm{d}v_\star,\\
&\rho_{f\star} = (1-\bar\phi\phi_\star), \qquad u_f(t,x) = \mathrm{U}\ u_{f\star}(t_\star,x_\star),\\
&\mu = \bar\mu\ \mu_\star(\phi_\star), \qquad Z = Z_\star(\phi_\star).
\end{aligned}$$

From now on, we skip the stars subscripts, having in mind that, unless explicitly mentioned, all the variables are understood as dimensionless ones . Endowed with these definitions, we are led to

$$\begin{aligned}
&\partial_t F + \eta\xi\cdot\nabla_x F + \frac{\bar g}{\eta}\cdot\nabla_\xi F = \frac{\mu(\phi)}{\epsilon}\nabla_\xi\cdot\big(Z(\phi)\ (\xi - u_f/\eta)F + \nabla_\xi F\big),\\
&\partial_t\rho_f + \nabla_x\cdot(\rho_f u_f) = 0,\\
&\partial_t(\rho_f u_f) + \mathrm{Div}_x(\rho_f u_f\otimes u_f) + \nabla_x p\\
&\qquad\qquad = \mathrm{Div}_x\big(2\mu\mathbb{D}(u_f)\big) + \rho_f\bar g + \frac{\bar\phi\bar\rho_d}{\epsilon\bar\rho_f}\ \mu(\phi)Z(\phi)\int_{\mathbb{R}^3}(\eta\xi - u_f)F\,\mathrm{d}\xi.
\end{aligned}$$

For the sake of simplicity, we have assumed that the units are such that the diffusion coefficient scales as $\frac{\bar\mu\mathrm{T}}{\bar\rho_f\mathrm{L}^2} = 1$. We are interested in regimes where $0 < \epsilon \ll 1$. It leads to relaxation processes since the particle distribution function is pushed to resemble a Maxwellian. This is reminiscent of hydrodynamic regimes in gas dynamics [63]. Indeed, the penalization of the Fokker–Planck operator drives F towards an element of the kernel of this operator:

$$F \simeq \mathcal{M}, \qquad \nabla_\xi\cdot\big(Z(\phi)\ (\xi - u_f/\eta)\mathcal{M} + \nabla_\xi\mathcal{M}\big) = 0,$$

which eventually means

$$\begin{aligned}
F(t,x,\xi) &\simeq \mathcal{M}(t,x,\xi)\\
&\simeq \phi(t,x)\ \Big(\frac{Z(\phi(t,x))}{2\pi}\Big)^{3/2}\ \exp\Big(-\frac{Z((\phi)(t,x))\ |\xi - u_f(t,x)/\eta|^2}{2}\Big).
\end{aligned}$$

However, the details of the asymptotics depends on the behavior of the other scaling parameters with respect to ϵ, which will be discussed in a while. In order to investigate the asymptotic behavior as ϵ tends to 0, it is convenient to introduce the following notation

$$\begin{pmatrix} \phi \\ J \\ \mathbb{P} \end{pmatrix} = \int_{\mathbb{R}^3} \begin{pmatrix} 1 \\ \eta\xi \\ \xi \otimes \xi \end{pmatrix} F \, \mathrm{d}\xi.$$

The moment equations now recast as follows

$$\begin{aligned} &\partial_t \phi + \nabla_x \cdot J = 0, \\ &\partial_t J + \eta^2 \mathrm{Div}_x \mathbb{P} - \bar{g}\phi = -\frac{\mu(\phi)Z(\phi)}{\epsilon}(J - \phi u_f). \end{aligned} \tag{22}$$

Of course, these relations are nothing but the dimensionless version of the evolution equations derived above for ρ_d and $\rho_d u_d$. Note that the system is not closed since the higher moment $\mathbb{P}$ cannot be expressed in general by means of ϕ and J. The equation for the fluid velocity becomes

$$\partial_t(\rho_f u_f) + \mathrm{Div}_x(\rho_f u_f \otimes u_f) + \nabla_x p = \mathrm{Div}_x\big(2\mu \mathbb{D}(u_f)\big) + \rho_f \bar{g} + \frac{\bar{\phi}\bar{\rho}_d}{\epsilon \bar{\rho}_f} \, \mu(\phi)Z(\phi) \, (J - \phi u_f).$$

In rescaled form the mean density of the mixture reads

$$\rho = \rho_f + \bar{\phi}\frac{\bar{\rho}_d}{\bar{\rho}_f}\phi$$

while the velocity of the mixture is defined by

$$\rho u = \rho_f u_f + \bar{\phi}\frac{\bar{\rho}_d}{\bar{\rho}_f} J.$$

Therefore, we are led to

$$\begin{aligned} &\partial_t \rho + \nabla_x \cdot (\rho u) = 0, \\ &\partial_t(\rho u) + \mathrm{Div}_x\Big(\rho_f u_f \otimes u_f + \bar{\phi}\frac{\bar{\rho}_d}{\bar{\rho}_f}\eta^2 \mathbb{P} + \nabla_x p\Big) = \mathrm{Div}_x\big(2\mu\mathbb{D}(u_f)\big) + \bar{g}\rho. \end{aligned}$$

In order to make diffusion effects appear in the evolution of the particles volume fraction, it is necessary to introduce the following scaling assumption

$$0 < \epsilon \ll 1, \qquad \bar{\phi}\frac{\bar{\rho}_d}{\bar{\rho}_f}\frac{1}{\epsilon} = \bar{\phi}\frac{\bar{\rho}_d}{\bar{\rho}_f}\eta^2 = 1$$

or, in other words

$$\eta = \frac{1}{\sqrt{\epsilon}} \gg 1, \qquad \bar{\phi}\frac{\bar{\rho}_d}{\bar{\rho}_f} = \epsilon \ll 1.$$

(In fact $\frac{\bar{\phi}}{\epsilon}\frac{\bar{\rho}_d}{\bar{\rho}_f}$ and $\bar{\phi}\frac{\bar{\rho}_d}{\bar{\rho}_f}\eta^2$ can be assumed to tend to any positive constants, the important fact being to impose the behavior with respect to ϵ.) Therefore, combining the relaxation effect induced by making the Fokker–Planck operator stiff to the velocity scaling, we expect as ϵ goes to 0 that the particles distribution function looks like a centered Maxwellian

$$F \simeq \frac{\phi}{(2\pi/Z(\phi))^{3/2}} e^{-Z(\phi)|\xi|^2/2}.$$

Accordingly the kinetic pressure becomes

$$\mathbb{P} = \int_{\mathbb{R}^3} \xi \otimes \xi F \, \mathrm{d}\xi \simeq \frac{\phi}{Z(\phi)} \mathbb{I}.$$

Taking into account the scaling assumption, the evolution of the first order moment is governed by

$$\epsilon \partial_t J + \mathrm{Div}_x \mathbb{P} - \epsilon \bar{g} \phi = -\mu(\phi) Z(\phi) \ (J - \phi u_f).$$

To describe the asymptotic behavior, we assume that the sequences of unknowns admit limit

$$\phi, J, u_f \to \Phi_\ell, J_\ell, u_\ell$$

in a strong enough sense so that we can pass to the limit in non linearities. We bear in mind that $\bar{\phi}$ remains a free scaling parameter; we assume that $\bar{\phi} \to \bar{\phi}_\ell$. Then, letting ϵ go to 0, we arrive at

$$\begin{aligned}
&\partial_t \Phi_\ell + \nabla_x \cdot J_\ell = 0, \\
&\nabla_x \left(\frac{\Phi_\ell}{Z(\Phi_\ell)} \right) - = -\mu(\Phi_\ell) \ Z(\Phi_\ell) \ (J_\ell - \Phi_\ell u_\ell).
\end{aligned}$$

Hence Φ_ℓ is solution of a nonlinear convection–diffusion equation

$$\partial_t \Phi_\ell + \nabla_x \cdot \Big(\Phi_\ell u_\ell - \frac{1}{\mu(\Phi_\ell) Z(\Phi_\ell)} \Big(\nabla_x \frac{\Phi_\ell}{Z(\Phi_\ell)} \Big) \Big) = 0.$$

Now, the mean density reads $\rho = (1 - \bar{\phi}\phi) + \epsilon\phi \to \rho_\ell = (1 - \bar{\phi}_\ell \Phi_\ell)$ and the mean velocity satisfies $\rho u = (1 - \bar{\phi}\phi) u_f + \epsilon J \to \rho_\ell u_\ell$. Then, the momentum equation becomes

$$\partial_t(\rho_\ell u_\ell) + \mathrm{Div}_x(\rho_\ell u_\ell \otimes u_\ell) + \nabla_x \Big(p_\ell + \frac{\Phi_\ell}{Z(\Phi_\ell)} \Big) = \mathrm{Div}_x \big(2\mu \mathbb{D}(u_\ell) \big) + \bar{g} \rho_\ell.$$

The mass conservation reads

$$\begin{aligned}
&\partial_t \rho_\ell + \nabla_x \cdot (\rho_\ell u_\ell) = 0 \\
&= -\bar{\phi}_\ell \big(\partial_t \Phi_\ell + \nabla_x \cdot (\Phi_\ell u_\ell) \big) + \nabla_x \cdot u_\ell = 0.
\end{aligned}$$

Then, we distinguish two situations:

- Either $\bar{\phi}_\ell = 0$, and thus $\rho_\ell = 1$; in such a case the velocity is merely divergence free $\nabla_x \cdot u_\ell = 0$,

- Or $\bar{\phi}_\ell > 0$: in such a case the velocity field is required to satisfy the constraint

$$\nabla_x \cdot u_\ell = \bar{\phi}_\ell \ \nabla_x \cdot \Big(\frac{1}{\mu(\Phi_\ell) Z(\Phi_\ell)} \Big(\nabla_x \frac{\Phi_\ell}{Z(\Phi_\ell)} \Big) \Big).$$

Further mathematical analysis of the asymptotics is beyond the scope of the present paper. We refer the reader to [38, 39] for technical details on such questions and to [41] for further applications to mixture flows.

Example 1 *A relevant situation corresponds to the case where we use the Einstein definition of the effective viscosity of the solution, see [26, 8]*

$$\mu(\phi) = \bar{\mu} \times \Big(1 + \frac{5}{2} \phi \Big).$$

Assuming $Z = 1$, $\bar{g} = 0$, *it yields*

$$\nabla_x \cdot u_\ell = \frac{2}{5} \Delta_x \ln \Big(1 + \frac{5}{2} \bar{\phi} \Phi_\ell \Big) = -\frac{2}{5} \Delta_x \ln \Big(\frac{7}{2} - \frac{5}{2} \rho_\ell \Big).$$

A relevant generalization of this simple law for the effective viscosity is proposed e. g. in [17]. Using the Stokes law for the drag force makes sense when the particle Reynolds number $\frac{2\rho_f |u_f - \mathrm{V}_{th}| a}{\mu}$ *is small. The simplest case with* $Z = 1$ *is used in many applications, see for instance [48, 53]. More complex examples have the form* $Z(\phi) = (1 - \phi)^{-\kappa}$, *see [60,* $\kappa = 2.8$ *in Eq. (7)], [3,* $\kappa = 2.65$ *in Eq. (5)] or [57].*

References

[1] T. Alazard. Low Mach number flows and combustion. *SIAM J. Math. Anal.*, 38:1186–1213, 2006.

[2] T. Alazard. A minicourse on the low Mach number limit. *Discrete and Continuous Dynamical Systems-Series S*, 3:365–404, 2008.

[3] M. J. Andrews and P. J. O'Rourke. The multiphase particle-in-cell (MP-PIC) method for dense particulate flows. *Int. J. Multiphase Flow*, 22(2):379–402, 1996.

[4] G. Ansanay-Alex. *Un schéma éléments finis non-conformes/volumes finis pour l'approximation en maillages non structurés des écoulements à faible nombre de Mach.* PhD thesis, Université de Provence, Aix-Marseille, France, 2009.

[5] S. N. Antontsev, A. V. Kazhikhov, and V. N. Monakhov. *Boundary value problems in mechanics of nonhomogeneous fluids*, volume 22 of *Studies in Math. and its Appl.* North Holland, 1990.

[6] H. Beirao da Veiga. Diffusion on viscous fluids. Existence and asymptotic properties of solutions. *Annali Scuola Norm. Sup. Pisa, Classe di Scienze*, 10:341–355, 1983.

[7] F. Boyer and P. Fabrie. *Mathematical Tools for the Study of the Incompressible Navier–Stokes Equations and Related Models*, volume 183 of *Applied Mathematical Sciences*. Springer, 2013.

[8] J. F. Brady. The Einstein viscosity correction in n dimensions. *Int. J. Multiphase Flow*, 10(1):113–114, 1983.

[9] H. Brenner. Unsolved problems in fluid mechanics: On the historical misconception of fluid velocity as mass motion, rather than volume motion, 2003. Communication for the 100th anniversary of the Ohio State Chemical Engineering Department.

[10] H. Brenner. Navier-Stokes revisited. *Phys. A*, 349(1-2):60–132, 2005.

[11] H. Brenner. Bi-velocity hydrodynamics: multicomponent fluids. *Internat. J. Engrg. Sci.*, 47:902–929, 2009.

[12] H. Brenner. Diffuse volume transport in fluids. *Phys. A*, 389:4026–4045, 2010.

[13] D. Bresch, El H. Essoufi, and M. Sy. Effect of density dependent viscosities on multiphasic incompressible fluid models. *J. Math. Fluid Mech.*, 9(3):377–397, 2007.

[14] C. Calgaro, E. Chane-Kane, E. Creusé, and T. Goudon. L^∞ stability of vertex-based MUSCL finite volume schemes on unstructured grids; simulation of incompressible flows with high density ratios. *J. Comput. Phys.*, 229(17):6027–6046, 2010.

[15] C. Calgaro, J.-P. Chehab, and Y. Saad. Incremental incomplete LU factorizations with applications to time-dependent PDEs. *Numer. Lin. Algebra with Appl.*, 17(5):811–837, 2010.

[16] C. Calgaro, E. Creusé, and T. Goudon. An hybrid finite volume-finite element method for variable density incompressible flows. *J. Comput. Phys.*, 227(9):4671–4696, 2008.

[17] N. S. Cheng and A. W. K. Law. Exponential formula for computing effective viscosity. *Powder Technology*, 129(1-3):156–160, 2003.

[18] S. Clain and V. Clauzon. L^∞ stability of the MUSCL methods. *Numer. Math.*, 116(1):31–64, 2010.

[19] R. Danchin. Density-dependent incompressible fluids in bounded domains. *J. Math. Fluid Mech.*, 8(3):333–381, 2006.

[20] R. Danchin and X. Liao. On the well-posedness of the full low-Mach number limit system in general critical Besov spaces. *Commun. Contemp. Math.*, 14(3), 2012. article # 1250022.

[21] C. Debiez, A. Dervieux, K. Mer, and B. Nkonga. Computation of unsteady flows with mixed finite volume/finite element upwind methods. *Internat. J. Numer. Methods Fluids*, 27(1-4, Special Issue):193–206, 1998.

[22] B. Desjardins. Global existence results for the incompressible density-dependent Navier-Stokes equations in the whole space. *Differential and Integral Equations*, 10:587–598, 1997.

[23] J. Droniou and C. Le Potier. Construction and convergence study of schemes preserving the elliptic local maximum principle. *SIAM J. Numer. Anal.*, 49(2):459–490, 2011.

[24] D. Dutykh, C. Acary-Robert, and D. Bresch. Mathematical modeling of powder-snow avalanche flows. *Stud. Appl. Math.*, 127(1):38–66, 2011.

[25] A. Einstein. On the motion of small particles suspended in liquids at rest required by the molecular-kinetic theory of heat. *Ann. Physik*, 17:549–560, 1905.

[26] A. Einstein. Eine neue bestimmung der moleküldimensionen. *Ann. Physik*, 19:289–306, 1906. Doctoral dissertation, Zurich, 1905.

[27] J. Etienne. *Simulation numérique directe de nuages aérosols denses sur des pentes ; application aux avalanches de neige poudreuse*. PhD thesis, Institut National Polytechnique de Grenoble, 2004.

[28] J. Etienne, E. J. Hopfinger, and P. Saramito. Numerical simulations of high density ratio lock-exchange flows. *Physics of Fluids*, 17, 036601, 2005.

[29] J. Etienne, M. Rastello, and E. Hopfinger. Modelling and simulation of powder–snow avalanches. *C. R. Acad. Sci., Mécanique*, 334:545–554, 2006.

[30] J. Etienne, P. Saramito, and E.J. Hopfinger. Numerical simulations of dense clouds on steep slopes : Application to powder-snow avalanches. *Ann. Glaciol.*, 38:379–383(5), 2004. Presented at IGS International Symposium on Snow and Avalanches. Davos, Switzerland 2-6 June 2003.

[31] R. E. Ewing, T. Lin, and Y. Lin. On the accuracy of the finite volume element method based on piecewise linear polynomials. *SIAM J. Num. Anal.*, 39(6):1865–1888, 2002.

[32] R. Eymard, T. Gallouët, and R. Herbin. Finite volume methods. In *Handbook of numerical analysis, Vol. VII*, Handb. Numer. Anal., VII, pages 713–1020. North-Holland, Amsterdam, 2000.

[33] R. Eymard, D. Hilhorst, and M. Vohralík. A combined finite volume-finite element scheme for the discretization of strongly nonlinear convection-diffusion-reaction problems on nonmatching grids. *Numer. Methods Partial Differential Equations*, 26(3):612–646, 2010.

[34] E. Feireisl and A. Vasseur. New perspectives in fluid dynamics: Mathematical analysis of a model proposed by Howard Brenner. In A. V. Fursikov, G. P. Galdi, and V. V. Pukhnachev, editors, *New Directions in Mathematical Fluid Mechanics. The Alexander V. Kazhikhov Memorial Volume*, Advances in Mathematical Fluid Mechanics, pages 153–179. Springer, 2010.

[35] M. Feistauer, J. Felcman, M. Lukáčová-Medvid̆ová, and G. Warnecke. Error estimates for a combined finite volume–finite element method for nonlinear convection-diffusion problems. *SIAM J. Numer. Anal.*, 36(5):1528–1548, 1999.

[36] F. Franchi and B. Straughan. A comparison of Graffi and Kazhikov–Smagulov models for top heavy pollution instability. *Adv. in Water Resources*, 24:585–594, 2001.

[37] V. S. Galkin and S. V. Rusakov. Kinetic Fokker–Planck equation for free-molecular, thermally nonequilibrium Brownian particles in an inhomogeneous gas. *Fluid Dynamics*, 42:330–334, 2007. Originally published in Izvestiya Rossiiskoi Akademii Nauk, Mekhanika Zhidkosti i Gaza, 2007, Vol. 42, No. 2, pp. 204–208 (in Russian).

[38] T. Goudon, P.-E. Jabin, and A. Vasseur. Hydrodynamic limit for the Vlasov-Navier-Stokes equations. I. Light particles regime. *Indiana Univ. Math. J.*, 53(6):1495–1515, 2004.

[39] T. Goudon, P.-E. Jabin, and A. Vasseur. Hydrodynamic limit for the Vlasov-Navier-Stokes equations. II. Fine particles regime. *Indiana Univ. Math. J.*, 53(6):1517–1536, 2004.

[40] T. Goudon and S. Krell. A DDFV scheme for incompressible Navier-Stokes equations with variable density. In *Finite Volumes for Complex Applications VII Elliptic, Parabolic and Hyperbolic Problems.* Springer, 2014.

[41] T. Goudon and A. Vasseur. On a model for mixture flows: Derivation, dissipation and stability properties. Technical report, Inria, 2014.

[42] D. Graffi. Il teorema di unicitá per i fluidi incompressibili, perfetti, eterogenei. *Rev. Unione Mat. Argentina*, 17:73–77, 1955.

[43] J. L. Guermond, P. Minev, and J. Shen. An overview of projection methods for incompressible flows. *Comput. Methods Appl. Mech. Engrg.*, 195(44-47):6011–6045, 2006.

[44] F. Guillén-González and J. V. Gutiérez-Santacreu. Unconditional stability and convergence of fully discrete schemes for $2d$ viscous fluids models with mass diffusion. *Math. of Comp.*, 77(263):1495–1524, 2008.

[45] K. Hutter and R. Greve. Two-dimensional similarity solutions for finite-mass granular avalanches with Coulomb and viscous-type frictional resistance. *J. Glaciol.*, 39:357–372, 1993.

[46] D. D. Joseph and Y. Y. Renardy. *Fundamentals of two-fluid dynamics. Part II: Lubricated Transport, Drops and Miscible Liquids*, volume 3 of *Interdisciplinary Applied Mathematics.* Springer-Verlag, New York, 1993. Mathematical theory and applications.

[47] A. V. Kazhikhov and S. Smagulov. The correctness of boundary value problems in a diffusion model in an inhomogeneous fluid. *Sov. Phys. Dokl.*, 22:249–250, 1977.

[48] G. Lavergne. Modélisation de l'écoulement multiphasique dans le propulseur à poudre P230 d'Ariane 5. Ile dOléron, 2004. Lecture Notes of the School of the Groupement Français de Combustion.

[49] X. Liao. *Quelques résultats mathématiques sur les gaz à faible nombre de Mach.* PhD thesis, Université Paris-Est, 2013.

[50] X. Liao. A global existence result for a zero Mach number system. *J. Math. Fluid Mech.*, 16(1):77–103, 2014.

[51] P.-L. Lions. *Mathematical topics in fluid mechanics. Vol. 1 : Incompressible models*, volume 3 of *Oxford Lecture Series in Mathematics and its Applications.* The Clarendon Press Oxford University Press, New York, 1996. Oxford Science Publications.

[52] P.-L. Lions. *Mathematical topics in fluid mechanics. Vol. 2 : Compressible models*, volume 10 of *Oxford Lecture Series in Mathematics and its Applications.* The Clarendon Press Oxford University Press, New York, 1998. Oxford Science Publications.

[53] J. Mathiaud. *Etude de systèmes de type gaz-particules.* PhD thesis, ENS Cachan, 2006.

[54] F. Naaim-Bouvet. *Approche macro-structurelles des écoulements bi-phasiques turbulents de neige et de leur interaction avec des obstacles.* Habilitation à diriger les recherches, Univ. Joseph Fourier, Grenoble, 2003.

[55] F. Naaim-Bouvet, M. Naaim, M. Bacher, and L. Heiligenstein. Physical modelling of the interaction between powder avalanches and defence structures. *Natural Hazards and Earth System Sciences*, 2:193–202, 2002.

[56] F. Naaim-Bouvet, S. Pain, M. Naaim, and T. Faug. Numerical and physical modelling of the effect of a dam on powder avalanche motion: Comparison with previous approaches. *Surveys in Geophysics*, 24:479–498, 2003.

[57] P. J. O'Rourke. *Collective drop effects on vaporizing liquid sprays.* PhD thesis, Princeton University, NJ, 1981.

[58] S. Pain. Simulation numérique de l'interaction entre une avalanche en aérosol et une digue d'arrêt. *Publication interne ENGEES/CEMAGREF*, 2002.

[59] N. A. Patankar and D. D. Joseph. Lagrangian numerical simulation of particulate flows. *Int. J. Multiphase Flow*, 27:1685–1706, 2001.

[60] N. A. Patankar and D. D. Joseph. Modeling and numerical simulation of particulate flows by the Eulerian–Lagrangian approach. *Int. J. Multiphase Flow*, 27:1659–1684, 2001.

[61] K. R. Rajagopal and L. Tao. *Mechanics of mixtures*, volume 35 of *Series on Advances in Math. for Appl. Sci.* World Scientific, 1985.

[62] M. Rastello and E. Hopfinger. Sediment–entraining suspension clouds: a model of powder–snow avalanches. *J. Fluid Mech.*, 509:181–206, 2004.

[63] L. Saint Raymond. *Hydrodynamic Limits of the Boltzmann Equation*, volume 1971 of *Lect. Notes in Math.* Springer, 2009.

[64] P. Secchi. On the initial value problem for the equations of motion of viscous incompressible fluids in the presence of diffusion. *Boll. Un. Mat. Ital. B (6)*, 1(3):1117–1130, 1982.

[65] P. Secchi. On the motion of viscous fluids in the presence of diffusion. *SIAM J. Math. Anal.*, 19(1):22–31, 1988.

[66] D. M. Snider, P. J. O'Rourke, and M. J. Andrews. Sediment flow in inclined vessels calculated using a multiphase particle-in-cell model for dense particle flows. *Int. J. Multiphase Flow*, 24:1359–1382, 1998.